Cell Reports

Article

Apocryphal FADS2 activity promotes fatty acid diversification in cancer

Graphical Abstract

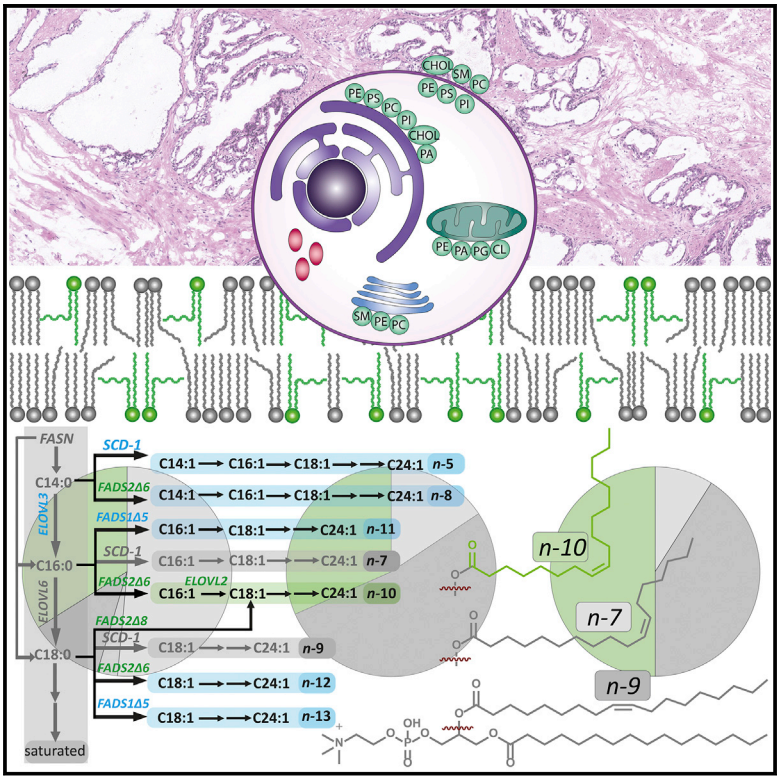

Highlights

- FADS2 promiscuity yields unreported families of fatty acids (i.e., *n*-8, *n*-10, and *n*-12)
- *n*-5 and *n*-13 fatty acids indicate apocryphal activities of SCD-1 and FADS1
- Unusual fatty acids display selective incorporation into phospholipid subclasses
- Distinctive enzyme-substrate interactions revealed in tumor tissue regions

Authors

Reuben S.E. Young, Andrew P. Bowman, Elizabeth D. Williams, ..., Ron M.A. Heeren, Martin C. Sadowski, Stephen J. Blanksby

Correspondence

martin.sadowski@pathology.unibe.ch (M.C.S.), stephen.blanksby@qut.edu.au (S.J.B.)

In Brief

Young et al. identify a wide array of unusual lipids in prostate cancer cell lines and tissues. Using isomer-resolved lipidomics in combination with gene silencing and stable-isotope tracing, the authors identify non-canonical desaturase and elongase enzyme activities driving increased diversification of fatty acid isomers.

Young et al., 2021, Cell Reports *34*, 108738
February 9, 2021
https://doi.org/10.1016/j.celrep.2021.108738

CellPress

Cell Reports

CellPress
OPEN ACCESS

Article

Apocryphal FADS2 activity promotes fatty acid diversification in cancer

Reuben S.E. Young,[1] Andrew P. Bowman,[2] Elizabeth D. Williams,[3] Kaylyn D. Tousignant,[3] Charles L. Bidgood,[3] Venkateswara R. Narreddula,[1] Rajesh Gupta,[4] David L. Marshall,[4] Berwyck L.J. Poad,[1,4] Colleen C. Nelson,[3] Shane R. Ellis,[2,5] Ron M.A. Heeren,[2] Martin C. Sadowski,[3,6,*] and Stephen J. Blanksby[1,4,7,*]

[1]School of Chemistry and Physics, Queensland University of Technology, Brisbane, QLD 4000, Australia
[2]M4I, The Maastricht MultiModal Molecular Imaging Institute, Division of Imaging Mass Spectrometry, Maastricht University, Universiteitssingel 50, 6229 ER Maastricht, the Netherlands
[3]Australian Prostate Cancer Research Centre—Queensland, Institute of Health and Biomedical Innovation, School of Biomedical Sciences, Faculty of Health, Queensland University of Technology (QUT), Princess Alexandra Hospital, Translational Research Institute, Brisbane, QLD 4000, Australia
[4]Central Analytical Research Facility, Institute for Future Environments, Queensland University of Technology, 2 George St., Brisbane, QLD 4000, Australia
[5]Molecular Horizons and School of Chemistry and Molecular Bioscience, University of Wollongong, Wollongong, NSW 2522, Australia
[6]Institute of Pathology, University of Bern, Murtenstrasse 31, 3008 Bern, Switzerland
[7]Lead contact
*Correspondence: martin.sadowski@pathology.unibe.ch (M.C.S.), stephen.blanksby@qut.edu.au (S.J.B.)
https://doi.org/10.1016/j.celrep.2021.108738

SUMMARY

Canonical fatty acid metabolism describes specific enzyme-substrate interactions that result in products with well-defined chain lengths, degree(s), and positions of unsaturation. Deep profiling of lipids across a range of prostate cancer cell lines reveals a variety of fatty acids with unusual site(s) of unsaturation that are not described by canonical pathways. The structure and abundance of these unusual lipids correlate with changes in desaturase expression and are strong indicators of cellular phenotype. Gene silencing and stable isotope tracing demonstrate that direct Δ6 and Δ8 desaturation of 14:0 (myristic), 16:0 (palmitic), and 18:0 (stearic) acids by FADS2 generate new families of unsaturated fatty acids (including *n*-8, *n*-10, and *n*-12) that have rarely—if ever—been reported in human-derived cells. Isomer-resolved lipidomics reveals the selective incorporation of these unusual fatty acids into complex structural lipids and identifies their presence in cancer tissues, indicating functional roles in membrane structure and signaling.

INTRODUCTION

Fatty acid (FA) metabolism is significantly altered within cancer cells, with increased FA unsaturation being pivotal in cell transformation, accelerated rates of proliferation, and augmented invasiveness (Beloribi-Djefaflia et al., 2016; Biswas et al., 2012; Currie et al., 2013; Röhrig and Schulze, 2016; Schulze and Harris, 2012; Zadra et al., 2013). The introduction of carbon-carbon double bonds (DBs) to specific sites along the FA chain is catalyzed by three distinct desaturase enzymes and results in structures with distinct physical properties and cellular functions (Renne and de Kroon, 2018). Alongside desaturation, elongation—a process that facilitates a two-carbon-unit chain extension through the elongase isoforms 1–7 (ELOVL1–7)—can also have profound effects on FA properties and function (Guillou et al., 2010). These now-modified FAs are usually incorporated into various complex lipids, such as phospholipids, whereby molecular properties are imparted to the functional role of the lipid, e.g., structural membrane packing (Lorent et al., 2020), fluidity (Scanferlato et al., 2019), and interleaflet interactions (Zhang and Lin, 2019), or specific signal transduction (Bratton et al., 1997; Epand, 2017; Hsu et al., 2013).

Previously, human prostate cancer (PCa) was shown to be characterized by increased ratios of monosaturated to saturated FAs relative to normal prostate tissue (Fritz et al., 2010). These metabolic expressions were supported by transcriptomics showing elevated mRNA levels for both stearoyl-coenzyme A (CoA) desaturase-1 (SCD-1) and ELOVL7 (Fritz et al., 2010; Tamura et al., 2009). Others have then focused on discerning the position of the DB in monounsaturated FAs and found that within malignant PCa cells, the abundance of FA 18:1*n*-9 (i.e., an 18-carbon monounsaturated FA with the DB in the 9th position from the methyl terminus) increases relative to the FA 18:1*n*-7 isomer compared with non-cancerous prostate cells (Ma et al., 2016b). Notably, it was recently shown that a secondary desaturation mechanism can be activated to meet the metabolic needs of cancer (Vriens et al., 2019). The canonical mechanism by which FAs undergo primary desaturation is through the oxygen-dependent SCD-1 enzyme introducing a DB at the Δ9 position (i.e., the 9th carbon from the FA carboxylate terminus). However, under cellular stress, fatty acyl desaturase 2 (FADS2)—a Δ6

desaturase—was also shown to possess primary desaturation capabilities, catalyzing *n*-10 DB formation in palmitic acid, which is a phenomenon usually observed only within lipids from hair and skin (Nicolaides, 1974). Having two independent mechanisms for primary desaturation creates the opportunity for plasticity in cancer cells, which carries potential functional consequences for membrane structure and signaling.

In order to elucidate if changes in unsaturation are widespread or confined to specific cellular functions, it is imperative to identify the unsaturation profiles of complex lipids and not just the FA building blocks. Unfortunately, technological limitations within conventional analysis, most notably gas chromatography, first require FAs to be released from complex lipids by hydrolysis. The resulting analysis provides a FA profile integrated across the entire lipid pool, leading to a reduction of molecular-level information of the lipidome and, moreover, dilution of low abundant FAs that may have a particular association with a specific lipid class or composition. To overcome these limitations, next-generation technologies for isomer-resolved lipidomics, such as Paternò-Büchi derivatization (Ma et al., 2016a) and ozone-induced dissociation (OzID); (Paine et al., 2018; Poad et al., 2010; Thomas et al., 2008), are instead able to discern DB positions within complex lipids. Such analyses not only provide links between unsaturation profiles and subcellular location or function but also create a platform in which lipid DBs can be imaged directly within a cellular-tissue matrix, revealing spatial distinctions between enzyme activities.

Here, we use isomer-resolved lipidomics in combination with small interfering RNA (siRNA) experiments and stable isotope tracing to reveal substrate promiscuity of the human FA desaturase FADS2. In combination with newly ascribed activity of the elongase ELOVL2, FADS2 gives rise to multiple FA families, namely *n*-8, *n*-10, and *n*-12 that have rarely—if ever—been reported in human-derived cells. These experiments also provide evidence for hitherto apocryphal activity of SCD-1 on 14:0 (myristic acid) and FADS1 modification of 18:0 (stearic acid), giving the cells access to an expanded repertoire of unsaturated FAs with *n*-5 and *n*-13 DBs. Furthermore, monounsaturated FAs within these *de-novo*-synthesized families are revealed as substrates for further desaturation and elongation, yielding a wide array of polyunsaturated FAs, including an isomer of FA 20:4*n*-6 (arachidonic acid), FA 20:4*n*-7. We demonstrate that these metabolites display selective and differential incorporation across different phospholipid classes related to membrane structure and signaling, which in turn can be used to uncover unique cellular phenotypes. Moreover, observing the distribution of these lipids through mass spectrometric tissue imaging improves our understanding of lipid metabolism in the tumor microenvironment by revealing distinct enzyme-substrate interactions in regions of tumor formation.

RESULTS

Widespread remodeling of unsaturation in cellular lipidomes

In order to explore the impact desaturase and elongase enzymes have on cellular FA metabolism, four PCa cell lines from metastatic deposits (PC-3, LNCaP, DU145, and VCaP; hereinafter referred to as cancer cells) and two benign immortalized prostate epithelial cell lines (BPH-1 and RWPE-1; hereafter referred to as normal prostate cells) were cultured under identical conditions. Representing the most in-depth lipidomic study of prostate cells to date, the cells were comprehensively characterized as follows: by conventional lipidomics to obtain full profiles of molecular phospholipids and neutral lipids (Table S2), allowing comparison between phospholipid classes (Figure 1A) and sum compositions, as shown for the dominant phosphatidylcholine (PC) class in Figure 1B; by isomer-resolved lipidomics (OzID) to reveal the contributions of isomers to the populations of monounsaturated lipid isomers (Tables S4 and S5), as shown for the most abundant lipid (PC 34:1, Figure 1C); by gas chromatography-mass spectrometry of the saponified extracts yielding the FA profile integrated over the lipid pool (Table S3); and by transcriptomics for fatty acyl desaturase expression (Figure 1D). Data represented in Figures 1A–1C were summarized using an unsupervised multivariate analysis in the form of principal-component analysis (PCA) (Figures 1E–1G) to differentiate cell line profiles.

PCA of the phospholipid profiles (Figure 1E) and the abundance of major PC lipids (Figure 1F) both reveal poor sample cluster separation, including cluster intermingling, and mixed adequacy in terms of the explanation of variance. This finding is seen where the phospholipid profile data (Figure 1E) can be reasonably explained by the first two principal components (~77%), whereas the variation in PC sum composition (Figure 1F) is weakly explained (~47%). Combined, these results indicate that conventional lipidomics contains unexplained factors of variation that contribute to an inability to distinguish cancer and normal prostate cell lines. Conversely, PCA of the DB isomer profiles from major monounsaturated PC species (Figure 1G) presents independent sample clustering, with the variation being well captured by the first two principal components (~81%). The clustering of PC-3, LNCaP, and VCaP cancer cell lines also displays strong negative association across both principal dimension axes against the normal prostate cell line BPH-1. Overall, multivariate analysis based on DB profiles clearly distinguishes between cancer and normal prostate cell lines (Figure 1G), whereas analogous analyses based on conventional lipidomics data are unable to do so (Figures 1E and 1F). Differentiation of cell lines based upon PCA of DB isomers is influenced strongly by the presence of unusual *n*-10 lipids. As evidenced in Figure 1C, PC 34:1*n*-10 contributions range from being absent in BPH-1 and VCaP cells to 50% of the isomer fraction in PC-3—remarkably representing up to 8.5 mol% of total phospholipid without impacting cell viability.

The high proportion of PC 34:1*n*-10 in some cell lines (Figure 1C, green) combined with the significant variation between unsaturation profiles (Figure 1G) implies change in the SCD-1 and FADS2 enzyme system. Although the delta-delta cycle threshold (ΔΔCT) mRNA measurements undertaken here inform of changes to enzyme mRNA transcription (Schmittgen and Livak, 2008), translation to proteins was not measured, and thus, changes in enzyme activity cannot be distinguished from enzyme abundance variation. Noting the absence of *n*-10, the BPH-1 normal prostate cell line was used as a reference to compare the transcription of SCD-1 and FADS2 mRNA across

CellPress
OPEN ACCESS

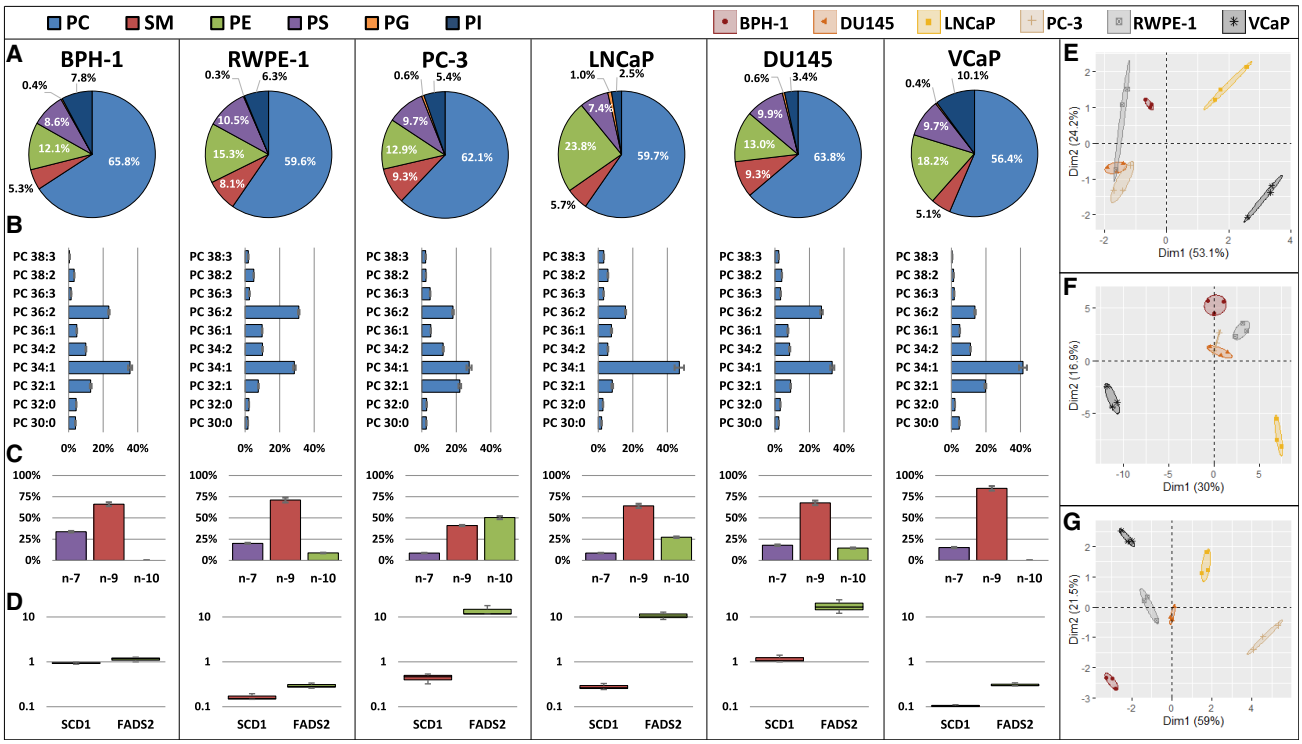

Figure 1. Lipid composition and targeted transcripts of normal prostate (BPH-1 and RWPE-1) and cancer (PC-3, LNCaP, DU145, and VCaP) cell lines

(A) Phospholipid profiles across 6 major classes (PC, sphingomyelin [SM], PE, PS, PG, and PI).

(B) Normalized abundance of major PC lipids quantified at the sum composition level.

(C) Normalized OzID signal intensity from PC 34:1 isomers with double bonds at *n*-7, *n*-9, and *n*-10.

(D) qRT-PCR-derived transcript expression of two desaturases (SCD-1 and FADS2) as a fold-change relative to normal prostate cell (BPH-1) mRNA expression.

(E–G) PCA dimensionality reduction for cell line differentiation based on 6 phospholipid classes (E), sum composition of 10 PCs (F), and double bond isomer distributions (G) from PC 32:1, 34:1, and 36:1. Ellipses display 95% confidence intervals, with the percentage of data represented by the dimensionality reduction being displayed as axes.

Data in (A)–(C) are displayed in relative totals for inter-cell line normalization. n = 3, mean ± SEM 95% confidence interval displayed.

all cell lines. Figure 1D shows a 10-fold increase in the transcription of FADS2 for the cancer cell lines PC-3, LNCaP, and DU145, where the contribution of *n*-10 unsaturation is most pronounced (Figure 1C, green). In contrast, RWPE-1 and VCaP cell lines present lower transcription of FADS2 (relative to BHP-1) and are characterized by a decreased abundance and complete absence, respectively, of the *n*-10 lipid isomer. Interestingly, these two cell lines also share a similar transcript expression of SCD-1 and FADS2 despite the clear difference in PC 34:1 DB isomer profiles (notably the absence of *n*-10 in VCaP). This apparent discrepancy between desaturase transcript expression and resulting metabolites points to competition between desaturase enzymes for common substrates with the potential for additional competition through substrate elongation. Such competition is also evident across the cell lines in the association between increased PC 34:1*n*-10 (Figure 1C, green) and decreased abundance of PC 34:1*n*-7 (Figure 1C, purple). Both isomers share 16:0 as a common substrate, and thus, competition between the independent SCD-1 or FADS2 reactions is apparent (Enoch et al., 1976; Ge et al., 2003). Similarly, observing the VCaP unsaturation profile relative to BPH-1 (Figure 1C), the decreased presence of PC 34:1*n*-7 (Figure 1C, purple) is matched by an increased abundance of PC 34:1*n*-9 (Figure 1C, red). As SCD-1 desaturation can yield either *n*-7 or *n*-9 FAs depending on the substrate (16:0 or 18:0, respectively), and ELOVL6 is known to elongate 16:0 to 18:0 (Jakobsson et al., 2006; Moon et al., 2001), the relative increase of VCaP PC 34:1*n*-9 suggests competitive 16:0 metabolism by either direct desaturation or a combination of elongation/desaturation reactions.

Given the potential for competition between desaturation and elongation pathways, the association between sites of unsaturation and specific fatty acyl chain length(s) becomes critical for mapping metabolism. Fatty acyl compositional analysis, based on collision-induced dissociation (CID) combined with OzID, reveals that cell line PC 34:1 is comprised of >95% PC 16:0_18:1 (Table S5), inferring that the vast majority of the *n*-7, *n*-9, and *n*-10 shown in Figure 1C are carried by 18:1 fatty acyl chains. Although somewhat varied, fatty acyl compositional analysis (based on negative polarity CID) of other lipid classes also revealed a majority contribution of 16:0_18:1 to the 34:1 species of phosphatidylinositol (PI), phosphatidylserine (PS),

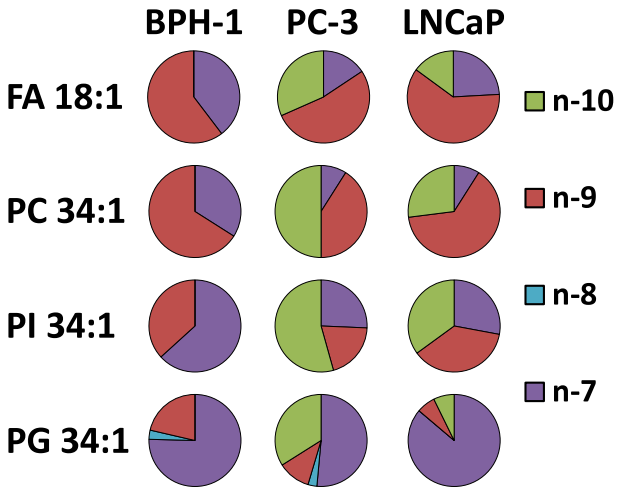

Figure 2. Variation of DBs across the hydrolyzed fatty acyl pool (GC-MS) and PC, PI, and PG (OzID) complex lipids for normal prostate BPH-1 cells and PC-3 and LNCaP cancer cells

The 16:0_18:1 fatty acyl composition comprises 95%, 78%, and 96% of total PC, PI, and PG 34:1 species, respectively. Increased *n*-10 can be observed within the cancer cell lines and, in some cases, represents over 50% of the phospholipid species. Mean values displayed (n = 3).

phosphatidylethanolamine (PE), and phosphatidylglycerol (PG), with average contributions of 78%, 58%, 77%, and 96%, respectively (Table S5). When exploring the DB positions tentatively assigned to the 18:1 chain of these phospholipids, however, the results show a large perturbation between cancer and normal prostate cells. Figure 2 displays the fractional contributions of DB isomers within three lipid subclasses across BPH-1 cells and PC-3 and LNCaP cancer cells. Because the majority of these monounsaturated lipids carry the 18:1 acyl chain, the isomer distribution of FA 18:1 from the hydrolyzed lipid pool was also derived from GC-MS (representative chromatograms shown in Figure S2).

The results summarized in Figure 2 highlight a significant contribution of FA 18:1*n*-10 to the total FA 18:1 pool in PC-3 (32%) and LNCaP (15%) cancer cell lines, whereas it is completely absent in the BPH-1 normal prostate cells. Any contribution of FA 18:1*n*-10 (or FA 16:1*n*-10; sapienic acid) from exogenous sources was explicitly excluded by rigorous analysis of cell culture media and other controls (Figure S2; Table S3). Comparing the isomer factions of FA 18:1 with the major 18:1-bearing lipids (i.e., PC 34:1, PI 34:1, and PG 34:1), two things become acutely apparent: (1) DB isomer proportions vary between phospholipid class (i.e., Figure 2, PC versus PI versus PG), and (2) the PG 34:1 of BPH-1 and PC-3 carries an additional *n*-8 isomer. These observations, which would be overlooked by pooled FA analysis alone, indicate a degree of specificity in the unsaturation profile across different phospholipid classes and the potential for greater diversity in lipid unsaturation than previously considered. Moreover, exploration of the DBs of triacylglycerols (TGs) and cholesteryl esters (CEs) reveals that this variation carries into the neutral lipid classes (Table S4). Remarkably, unusual fatty acyl DB isomers, such as 18:1*n*-10, are carried by neutral lipids in cell lines where the same acyl chain isomers are absent within phospholipid fractions. Consistent with the findings of previous research (Guijas et al., 2016), the signaling molecule and β-oxidation product of oleic acid 16:1*n*-9 was also identified in the neutral lipid fractions.

Expanded substrate accommodation of elongase and desaturase enzymes

Although a major contributor to the lipid pool for cancer cell lines, the biosynthetic origin of the FA 18:1*n*-10 building block remains to be clarified. The association of 18:1*n*-10 with the FADS2 desaturase is apparent (cf. Figure 1), and the canonical pathway would proceed by Δ6-desaturation of 16:0 to 16:1*n*-10 with subsequent elongation by a hitherto unassigned enzyme. To identify this elongase (hereinafter referred to as ELOVLx) along with other mechanisms for cancer cell plasticity, the LNCaP cancer cell line was chosen as a model based on its high expression of FADS2 and *n*-10 abundance. Cells were subject to gene silencing by siRNA and enzyme inhibition (Western blot, qRT-PCR, cell confluence and cell assay titrations in Figure S3) before monounsaturated phospholipids were characterized by OzID.

Relative to the untreated LNCaP control, the heatmap of Figure 3A displays DB assignments for 29 monounsaturated phospholipids and their abundance shift in response to treatment with desaturase gene silencing (siSCD-1 and siFADS2); elongase gene silencing (siELOVL3, siELOVL6, and siELOVL2); and a FADS2 inhibitor (SC26196—a potent FADS2 inhibitor that was found to prevent the conversion of linoleic acid to arachidonic acid by ≥95%) (Obukowicz et al., 1998). ELOVL3, ELOVL6, and ELOVL2 were chosen as they broadly represent canonical elongation activity for saturated, monounsaturated, and polyunsaturated fatty acyl substrates, respectively (Green et al., 2010; Guillou et al., 2010; Jakobsson et al., 2006). Based on previously established FA modification pathways, Figure S4 lays out the conceptual implications of preventing enzyme activities. Horizontal cluster grouping in Figure 3A reveals that desaturase treatments have a similar impact on phospholipids, whereas elongase treatments are separately grouped. Notably, the impact siELOVL2 treatment has on phospholipids is distinctive from that of siELOVL3 and siELOVL6, representing that ELOVL2 has a unique impact on the desaturation and elongation of phospholipid FAs.

Observing the vertical cluster analysis of Figure 3A identifies two main groups that correspond to SCD-1-related (i.e., predominately *n*-7 and *n*-9) and FADS2-related (i.e., predominately *n*-10) lipid products, e.g., PG 32:1*n*-7 and PG 32:1*n*-10 display inverse abundance shifts with the silencing of SCD-1 and FADS2 and hence are clustered separately. It is important to note that gene silencing restrict new FA progeny from being formed but do not remove prior-formed FAs from the cellular pool. Exchange of FAs between complex lipids, such as between phospholipids and neutral lipids, could account for the non-intuitive responses of some individual phospholipids to silencing treatments, e.g., increased PG 34:1*n*-10 abundance with siFADS2 and SC26196 treatments and no change in PE 36:1*n*-9 despite silencing SCD-1. For this reason, trends in unsaturation and FA chain elongation need to be assessed across the lipid pool and not restricted to individual species.

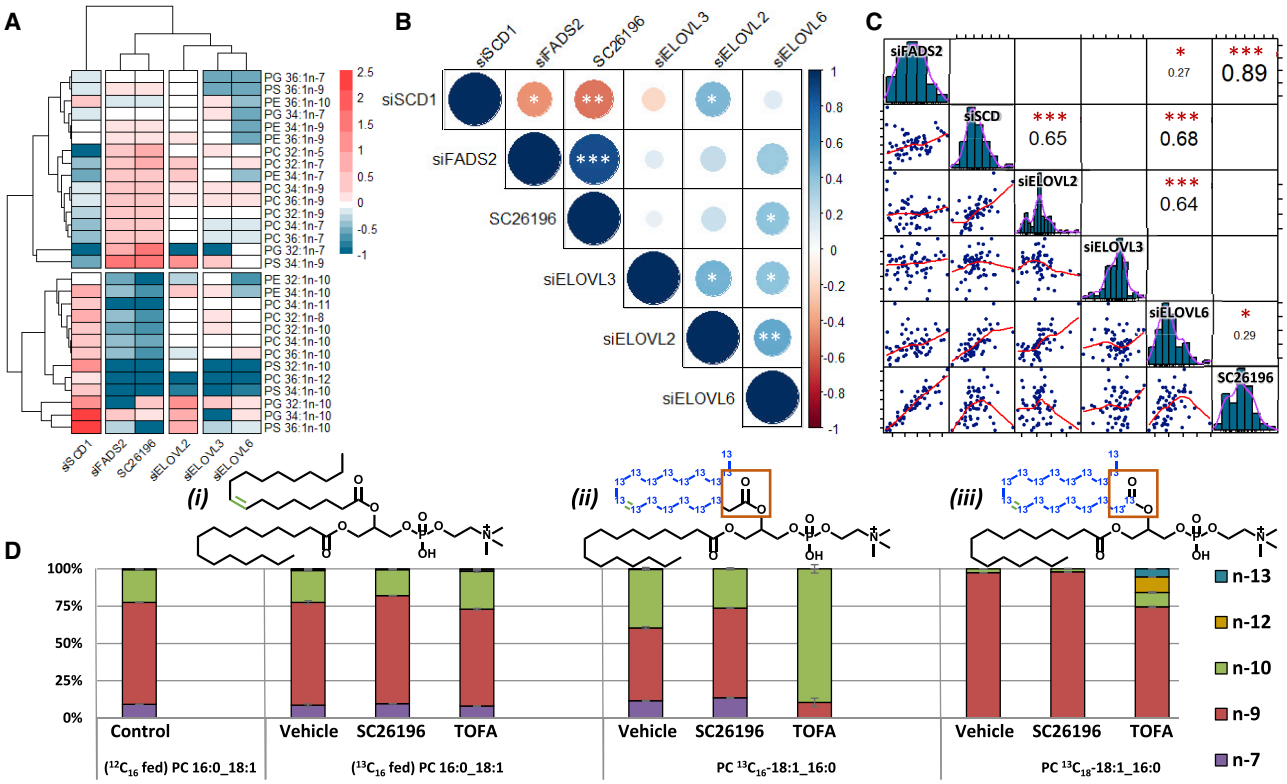

Figure 3. Enzyme/metabolite correlations and increased enzyme plasticity

(A) Heatmap of treated LNCaP cells showing change in monounsaturated phospholipid DB isomers relative to control (untreated LNCaP). Scale bar indicates fold change relative to untreated LNCaP control.

(B) Correlation matrix using numeric data from (A) to show positive (blue) and negative (red) correlations (n = 29).

(C) Bivariate analysis, histograms, and correlation matrices for treated LNCaP lipid sum compositional analysis compared with those of control (n = 60). Scale bar indicates positve/negative correlation coefficient values.

(D) PC 34:1 double bond fractional distribution profile from *de novo* lipogenisis (left and mid-left), $^{13}C_{16}$-palmitate tracing with *de novo* ^{12}C-acyl-CoA modifications (mid-right), and $^{13}C_{18}$-stearate tracing (right). Lipid structures are displayed above, with ^{13}C-carbons in blue (n = 2, mean ± SEM 95% confidence interval error bars). Pearson's correlation with two-tailed t test used for displayed correlation coefficients; *p ≤ 0.05, **p ≤ 0.01, ***p ≤ 0.001.

To observe statistical correlations between the monounsaturated lipid profiles generated in response to treatments (Figure 3A), Pearson's correlation was implemented, and the resulting correlation matrix is presented in Figure 3B. Notably, the inverse relationship between siFADS2 and siSCD-1 identified previously in Figure 3A is observed in Figure 3B to have statistically significant negative correlations ($p < 0.05$ and $p < 0.01$, respectively). Similar to the horizontal hierarchical clusters of Figure 3A, the desaturase and elongase treatments group separately at the top and bottom matrix vertices, indicating similarity in response to like-enzyme treatments. Given the increased FADS2-related products with siSCD-1 treatment (cf. Figure 3A), to identify ELOVLx, correlations between siSCD-1 and an siELOVL treatment are required. Within the matrix region corresponding to the correlation of desaturase treatment profiles to elongase enzyme treatment profiles, only two statistically significant positive correlations can be observed between desaturases and elongases, namely, siSCD-1/siELOVL2 and SC26196/siELOVL6.

As previously mentioned, a canonical activity of ELOVL6 is elongation of 16:0 to 18:0 (Jakobsson et al., 2006); therefore, downregulation of this activity by siELOVL6 treatment would cause accumulation of 16:0, palmitic acid. To prevent palmitic acid lipotoxicity, canonical activity of SCD-1 would drive desaturation to FA 16:1*n*-7 (Collins et al., 2010). Likewise, inhibition of the FADS2 enzyme by SC26196 would prevent palmitic acid from undergoing FADS2 desaturation to FA 16:1*n*-10 and instead consolidate desaturation activity through SCD-1, creating increases in FA 16:1*n*-7. These two paths leading to increased FA 16:1*n*-7 abundance would in turn present a positive correlation between siELOVL6 and FADS2 inhibition (SC26196). The silencing of SCD-1 desaturation (and hence increased abundance of monounsaturated FADS2 related lipid products), however, has no reported reason to display positive correlation to siELOVL2, as ELOVL2 has only been implicated in polyunsaturated FA elongation. Given that the silencing of ELOVLx would prevent the elongation of FA 16:1*n*-10 to FA 18:1*n*-10, the accumulation FA 16:1*n*-10 would display positive

correlation with a profile dominated by FADS2-related products, such as with siSCD-1. Consistently, this decreased 18:1*n*-10 formation can be observed within targeted PC 32:1 and PC 34:1 DB and FA compositions analyses (cf. Figure S6). Therefore, it is suggested that ELOVL2 is indeed ELOVLx and is responsible for the elongation of FA 16:1*n*-10 to FA 18:1*n*-10.

Akin to the major role of the FADS2 enzyme in polyunsaturated lipid synthesis, ELOVL2 has only previously been implicated in polyunsaturated fatty acyl elongation but never in the elongation of monounsaturated FAs (Jakobsson et al., 2006; Pauter et al., 2014). In order to validate the finding that ELOVL2 catalyzes elongation of FA 16:1*n*-10 to FA 18:1*n*-10, exploration into the impact of treatment on the wider lipidome was conducted. Relative to the control, Figure 3C displays the correlations between the lipid profiles of treatments, consisting of 60 saturated, monounsaturated, and polyunsaturated sum composition phospholipids (PC, PE, PS, and PG). As before in Figure 3B, the siELOVL2 and siELOVL6 treatments of Figure 3C display statistically significant positive correlations to desaturase silencing and inhibition, informing of moderate-to-high degrees of lipid profile similarity (0.65, $p \leq 0.001$ and 0.27, $p \leq 0.05$, respectively). Additionally, the profile from siELOVL6 also shows correlation with the siSCD-1 treatment profile (0.68, $p \leq 0.001$). Similar to the logic used previously, accumulation of 16:0 (palmitic acid) by way of silencing ELOVL6 would lead to an increase in shorter-chain monounsaturated lipids, which as substrates for further desaturation, would in turn increase the abundance of polyunsaturated lipids. Comparably, silencing SCD-1 would increase FADS2 activity, which would increase polyunsaturated lipid abundance due to its major canonical role in polyunsaturated lipid synthesis. Hence, the profiles of siELOVL6 and siSCD-1 would present similarly.

Although slight skewing can be observed, all histograms in Figure 3C present a normal distribution of the data, with the exception of siELOVL2. This bimodal distribution suggests that silencing of ELOVL2 has two distinctive impacts on the lipidome, which given its known role in the elongation of polyunsaturated lipids, provides further indication for an additional metabolic role by ELOVL2. Therefore, the combined data from Figures 3B, 3C, and S6 suggest that ELOVL2 is the most likely candidate for the unassigned elongase responsible for apocryphal elongation of 16:1*n*-10.

To explore the sequence of elongation and desaturation events, LNCaP cancer cells were supplemented with ^{13}C-labeled FAs. Incorporation of $^{13}C_{16}$-palmitate and $^{13}C_{18}$-stearate tracers into PC $^{13}C_{16}$-18:1_16:0 (*m/z* 798) and PC $^{13}C_{18}$-18:1_16:0 (*m/z* 800), respectively, was confirmed by high-resolution tandem MS (see data archive). The presence of PC $^{13}C_{16}$-18:1_16:0 (*m/z* 798) arising from $^{13}C_{16}$-palmitate supplementation indicates intracellular elongation with installation of two unlabeled carbons (cf. chemical structures, Figure 3Dii). This conclusion is supported by OzID of the mass-selected isotopologue that assigns the location of the two unlabeled methylene units between the site of unsaturation and the carboxylate moiety (cf. Table S6). The PC $^{13}C_{16}$-18:1_16:0 metabolite is also characterized by a distribution of sites of unsaturation in the labeled 18:1 chain showing contributions from *n*-7, *n*-9, and *n*-10 isomers (Figure 3Dii, left). In contrast, the fully labeled PC $^{13}C_{18}$-18:1_16:0 derived from $^{13}C_{18}$-stearate is characterized by near-exclusive *n*-9 unsaturation in the labeled chain (Figure 3Diii, left). These tracer results infer direct desaturation of stearate giving rise to 18:1*n*-9, whereas 18:1*n*-10 follows a desaturation-elongation sequence analogous to the canonical formation of 18:1*n*-7. Within the same experimental system, the suppression of *n*-10 unsaturation in PC $^{13}C_{16}$-18:1_16:0 was observed upon the inhibition of FADS2 (SC26196), further demonstrating Δ6-desaturation of palmitate prior to elongation (Figure 3Dii, mid). In contrast, inhibition of the same enzyme in the presence of the $^{13}C_{18}$-stearate tracer yields no observable change to the unsaturation profile of PC $^{13}C_{18}$-18:1_16:0 relative to vehicle (Figure 3Diii, mid) and corroborates direct desaturation by SCD-1 to form *n*-9. For comparison, the inhibition of SCD-1 (TOFA, originally an ACC1 inhibitor found to have potent SCD-1 inhibition) (Mason et al., 2012) in the presence of the $^{13}C_{16}$-palmitate tracer led to complete depletion of *n*-7 and a significant reduction of *n*-9 within PC $^{13}C_{16}$-18:1_16:0, indicating the cessation of Δ9-desaturation of palmitate and stearate, respectively—an effect that appears to trigger compensation through desaturation by FADS2, yielding an unsaturation profile dominated by *n*-10 (Figure 3Dii, right). Such compensation is also observed when inhibiting SCD-1 in the presence of the $^{13}C_{18}$-stearate tracer, which noticeably reduces *n*-9 unsaturation within PC $^{13}C_{18}$-18:1_16:0 and promotes formation of an unusual suite of *n*-13, *n*-12, and *n*-10 isomers indicative of direct Δ5-, Δ6-, and Δ8-desaturation of the tracer, respectively (Figure 3Diii, right).

Given the well-described Δ9-fidelity of SCD-1 (Bai et al., 2015), these results represent evidence for direct desaturation of stearate by desaturases other than SCD-1. Specifically, the findings demonstrate that 18:1*n*-10 can be synthesized directly from stearate by the hitherto apocryphal Δ8-desaturation activity of FADS2. Although Δ8 desaturases do occur naturally in some marine micro algae (Wallis and Browse, 1999), mammalian Δ8-desaturation of saturated FAs has only been observed exogenously on skin (Nicolaides, 1974). From the isotope labeling experiments above, the presence of *n*-12 accompanying *n*-10 monounsaturation within PC $^{13}C_{18}$-18:1_16:0 reveals that FADS2 may also be able to simultaneously exhibit Δ8-desaturation activity alongside canonical Δ6 activity. This result could indicate differential activities of the FADS2 enzyme arising from intracellular compartmentalization, local macrostructural environment, or substrates (i.e., carrier of the stearates). The proclivity of FADS1 (a third mammalian desaturase) toward Δ5 activity within polyunsaturated FAs may help explain the curious observation of the *n*-13 monounsaturated PC $^{13}C_{18}$-18:1_16:0. In this instance, however, the desaturase would require exertion of apocryphal metabolic behavior to instead act upon saturated substrates at the Δ5 position to initiate primary desaturation. This same Δ5 motif is observable in Figure 3A, wherein gene silencing of SCD-1 or FADS2 causes respective amplification or elimination of an unusual PC 34:1*n*-11. This variable presence may be explainable by Δ5-desaturation of 16:0 (palmitic acid) substrates by FADS1 during times of lesser competition for substrate by SCD-1.

Evidence for alternate pathways in lipid desaturation

An analysis of monounsaturated phospholipids within PCa cell lines revealed an unexpected diversity of lipid isomers

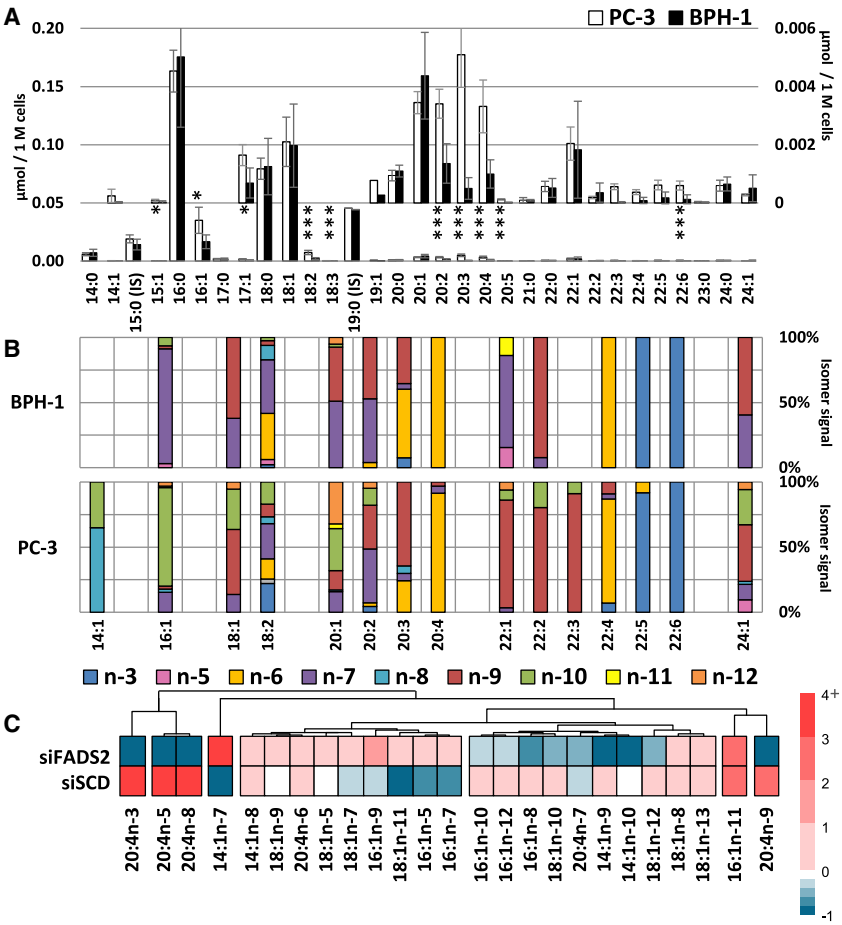

Figure 4. Pooled fatty acyl quantitation and double bond analysis of normal prostate cells (BPH-1), cancer cells (PC-3), and gene silencing of desaturases in cancer cells (LNCaP)

(A) Cell-count-normalized quantitative sum composition fatty acyl analysis with magnification insert (n = 3; mean ± SEM 95% confidence interval error; two-tailed Welch's t test used for p values: *$p \leq 0.05$, **$p \leq 0.01$, ***$p \leq 0.005$).

(B) Fractional distribution profiles for 15 mono- and polyunsaturated fatty acids from the hydrolyzed lipid pool (n = 3; mean fractional distribution displayed).

(C) Heatmap of treated LNCaP cells showing change in mono- and polyunsaturated fatty acid isomers from the hydrolyzed lipid pool (relative to LNCaP control). Scale bar indicates fold change relative to untreated LNCaP control. Annotated mass spectra of the unusual AMPP 20:4 species observed can be found alongside raw data files in the data archive.

(*vide supra*). To visualize this diversity across the entire fatty acyl pool, cell line extracts were hydrolyzed, derivatized with 1-[4-(aminomethyl)phenyl] pyridinium (AMPP+), and subjected to OzID. This direct-infusion MS approach was found to be more sensitive to low-abundant FAs and enabled unambiguous assignment of positions in the absence of reference standards (Poad et al., 2019). Comparison of AMPP+ against GC-MS results can be found in Figure S2. Figure 4A displays molar abundance of sum composition FAs for the two representative cell lines PC-3 (cancer) and BPH-1 (normal prostate) across three orders of magnitude. When isomeric contributions are ignored, the abundance of the saturated and monounsaturated FAs are well conserved between cell lines. In contrast, several low-abundant polyunsaturated FAs show significant changes in cellular abundances, e.g., FA 20:3, FA 20:4, and FA 22:6 are more abundant in PC-3 than in BPH-1.

As was observed within phospholipids, ostensibly similar sum composition profiles can mask significant isomeric differences (cf. Figure 1; Table S2). Fatty acyl isomer profiles were thus extracted from OzID analysis and are presented in Figure 4B. Among the monounsaturated even-chain FAs of PC-3, the apocryphal elongation of FA 16:1*n*-10 to FA 18:1*n*-10 that has been shown throughout appears not to be a terminal step in the elongation of the *n*-10 family. Instead, this family includes longer-chain FAs, such as 20:1, 22:1, and 24:1, representing successive chain elongation (*vide infra* Figure 5*vi*). Alongside further elongation of FA 18:1*n*-10 substrates, the presence of FA 18:2*n*-10, the skin lipid sebaleic acid, indicates the possibility for additional desaturation using this same FA 18:1 substrate and demonstrates a point of divergence in enzymatic activity surrounding the FA 18:1*n*-10. Further combinations of elongation and desaturation of FA 18:2*n*-10 subsequently lead to additional *n*-10 polyunsaturated fatty acyl species observed within FA 20:2, FA 22:2, and FA 22:3 (Figure 4B; *vide infra* Figure 5*vii*). A similar enzyme branch point can be observed with FA 18:1*n*-7, whereby the presence of *n*-7 isomers within FA 20:1, FA 22:1, and FA 24:1 (*vide infra* Figure 5*iv*) indicates elongation, whereas *n*-7 contributions to polyunsaturated FA 18:2, FA 20:2, FA 20:3, FA 20:4, and FA 22:4 demonstrate competitive elongation and desaturation (Figure 4B; *vide infra* Figure 5*iv*). These polyunsaturated FAs identified in PC-3 (and LNCaP; cf. Table S4) are remarkable not only because their biosynthetic origins and DB modifications are achieved solely through cellular mechanisms but also because they bear structural similarity to dietary-derived, biologically active FAs, such as arachidonic acid and adrenic acid.

The multiple isomeric species observed within the FA 20:4 profile of PC-3 in Figure 4B, including FA 20:4*n*-7, an isomer also seen within PI 38:4*n*-7 of PCa tissues and cell lines (cf. Figure 6C), and their absence from normal prostate BPH-1 cells represent an overall increase in the isomer diversity of polyunsaturated FAs in PC-3 and other cancer cell lines (cf. Table S4). This increased isomeric complexity of polyunsaturated fatty acyl profiles appears to correspond with an increase in isomer speciation created during the primary desaturation of shorter-chain saturated FAs (i.e., FA 14:0, FA 16:0, and FA 18:0) and can be clearly

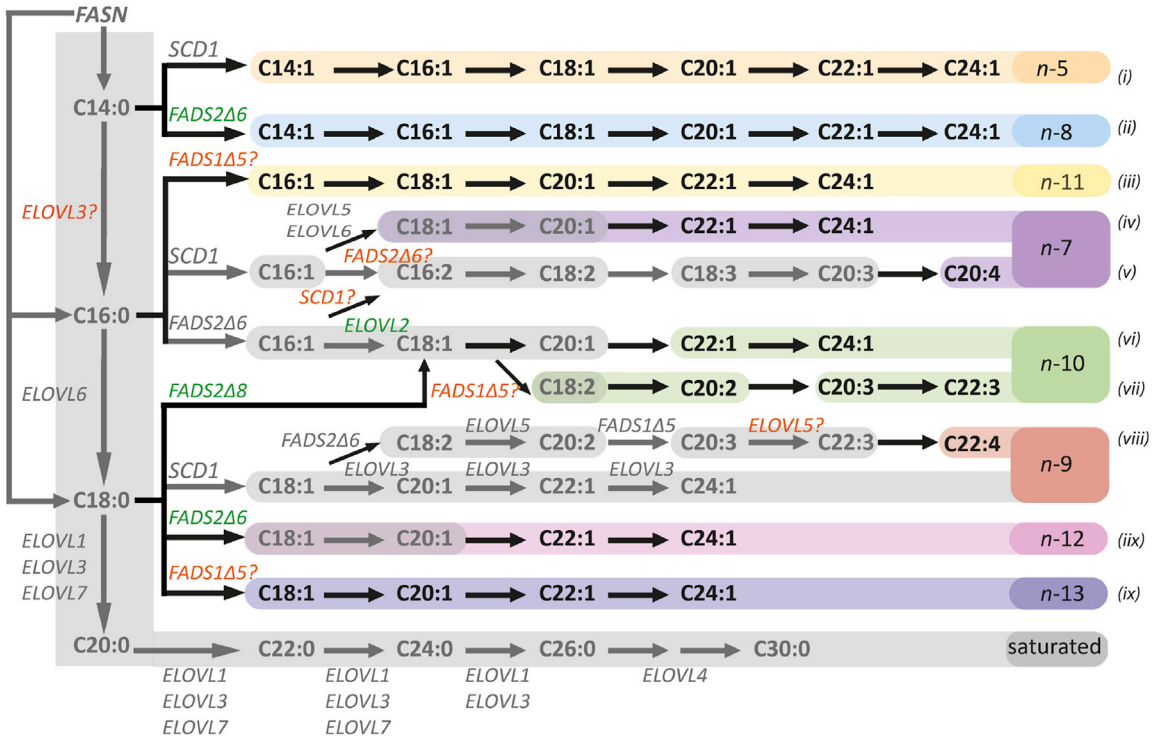

Figure 5. Fatty acyl desaturase and elongase pathways rationalizing the fatty acyl species observed within this study

Gray shading shows previously defined pathways (Guillou et al., 2010), and colored pathways show unusual FA species found in human prostate cell lines. Gray text represents known possibilities for mammalian enzyme activity, green text shows confirmed enzyme results for human prostate cell lines, and orange text displays enzymes requiring further confirmation.

observed with desaturase gene silencing (Figure 4C). Relative to the untreated LNCaP control, gene silencing of cellular FADS2 decreases the isomeric complexity of monounsaturated FA 14:1, FA 16:1, and FA 18:1 by heavily reducing the presence of *n*-8, *n*-10, and *n*-12 isomers while simultaneously eliminating of FA 20:4*n*-7 and consolidating the FA 20:4 profile in FA 20:4*n*-6, arachidonic acid. Conversely, the FA profile from SCD-1 gene silencing appears to have greater isomeric speciation within FA 14:1, FA 16:1, and FA 18:1, which in turn has no impact on polyunsaturated FA 20:4 isomer complexity, as both FA 20:4*n*-7 and FA 20:4*n*-6 are found to be present.

The expanded isomeric complexity afforded by apocryphal primary desaturation also creates an array of unusual monounsaturated FAs, which individually infer explicit enzyme-substrate activity that can be organized into a network of metabolites (Figure 5). For example, FA 24:1*n*-5, which is present in the FAs of PC-3 in Figure 4B, is consistent with canonical SCD-1 Δ9-desaturation of FA 14:0 to initially yield FA 14:1*n*-5 along with other chain length intermediates in this *n*-5 family (Figure 5*i*; Table S4). In another example of divergent enzyme action, this same FA 14:0 substrate is seen to undergo Δ6-desaturation by FADS2 to form FA 14:1*n*-8, a product that is observed within PC-3 (Figure 4B) and is highly sensitive to gene silencing of FADS2 (Figure 4C). The presence of this DB position in various chain lengths (see Table S4) indicates that this family of FAs has the ability to extend to at least FA 24:1 (Figure 5*ii*) and has the potential for incorporation into intact phospholipids (cf. Figure 2). Shifting to FA 18:0 as a substrate, FADS2 Δ6-desaturation yields FA 18:1*n*-12, which along with the 20:1, 22:1, and 24:1, is a FA family that can be observed in the FAs of PC-3 (Figures 4B and 5*iix*). The 18:1*n*-12, is also seen to form under SCD-1 inhibition of intact lipids with incorporated heavy-labeled FAs (cf. Figure 3D) and shows sensitivity to FADS2 gene silencing with apparent decreases relative to the control (Figure 4C).

Seemingly beyond the reported Δ9 and Δ6 positional activities for primary desaturation by SCD-1 or FADS2, two additional monounsaturated FA families can be observed in Figures 4B and 4C, namely, *n*-11 and *n*-13 (cf. Figures 3A and 3D). The emergence of both of these families is consistent with Δ5 primary desaturation of either FA 16:0 or FA 18:0 substrates to initially yield FA 16:1*n*-11 and FA 18:1*n*-13, respectively, before chain elongation with intermediates observed out to FA 24:1 (*cf.* Table S4; Figures 5*iii* and 5*ix*). Although no mammalian desaturase has been reported to facilitate Δ5 primary desaturation for the synthesis of monounsaturated FAs, Δ5-desaturation is commonplace during the synthesis of polyunsaturated FAs and undertaken by FADS1. Notably, both FADS1 and FADS2 are genetically coded by the same region on chromosome 11q12-q13.1 and share remarkable similarity in their exon/intron structure and nucleotide position for boundary disruption and a high degree of polypeptide sequence identity (Marquardt et al., 2000). This same region has been associated with single-

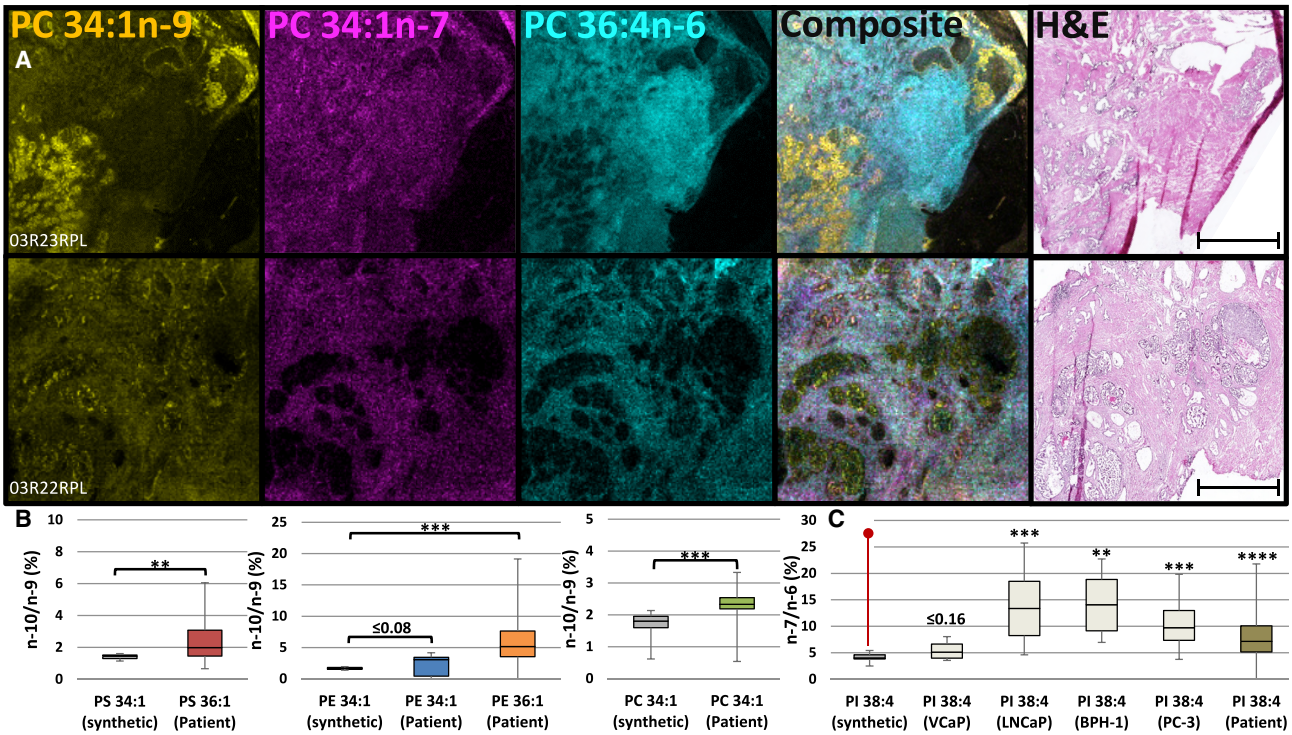

Figure 6. Metabolic differentiation of tumor in human prostate tissue

(A) Two separate patient prostate lobe sections showing (left to right) MALDI-MSI-OzID distribution of PC 34:1*n*-9 (yellow), PC 34:1*n*-7 (magenta), and PC 36:4*n*-6 (cyan); a composite image of these lipids; and the adjacent tissue section H&E stained. Magnification of tumor regions is shown; full images and spectral comparisons are found in Figure S1.

(B) False-positive *n*-10 signal arising from *n*-9 standards (gray) compared with tissue lipid extracts from both prostate lobes of 8 patients (n = 16); comparisons include PS 36:1*n*-10 (red), PE 34:1*n*-10 (blue), PE 36:1*n*-10 (orange), and PC 34:1*n*-10 (green).

(C) *n*-7 Signal arising from PI 38:4*n*-6 standard (gray/red line marker), four PCa cell lines (white), and tissue lipid extracts from both prostate lobes of 8 patients (n = 16; gold). The p values compare biologically occurring PI 38:4*n*-7 against false-positive *n*-7 signal from synthetic PI 38:4*n*-6 standard (red line marker). Scale bar: 2.60 mm. n ≥ 3 (standards), n = 3 (cell lines), and n = 16 (tissues); one-tailed Welch's *t*-test used for p values: **p ≤ 0.01, ***p ≤ 0.005, and ****p ≤ 0.0001.

nucleotide polymorphisms, DNA methylation, and alternate splicing—features that are known to alter the expression and translation of DNA (He et al., 2018; Park et al., 2012). Given the evidence (1) that FADS2 has the ability to exhibit high degrees of plasticity, (2) that the DNA within chromosome 11q12-q13.1 has the propensity to undergo changes, (3) of the gene sequence similarity between FADS1 and FASDS2, and (iv) of prior established changes to FADS1 activity (Park et al., 2018), it is speculated that, similar to FADS2, FADS1 is exhibiting plasticity by apocryphal Δ5 primary desaturation to form both *n*-11 and *n*-13 FA families.

Lipid unsaturation profiles in human prostate tissue

Lipid unsaturation distributions in human prostate sections were mapped using OzID coupled with matrix-assisted laser desorption ionisation MS imaging (MALDI-MSI). Figure 6A presents a spatial distribution between the monounsaturated phosphatidylcholine isomers PC 34:1*n*-9 (yellow) and PC 34:1*n*-7 (magenta), which are both metabolites of SCD-1, and the polyunsaturated PC 36:4*n*-6 (cyan), a metabolite formed through dietary FA substrates and FADS2 interactions. Comparison to the hematoxylin and eosin (H&E) stains of adjacent tissue sections reveals an increase of PC 34:1*n*-9 and a corresponding decrease of PC 36:4*n*-6 specific to the tumorous regions of the tissue. As these two metabolites are representative of two different desaturase enzyme activities, they are indicative of a change in substrate-enzyme interactions between tumor and adjacent non-tumor cells. The two PC 34:1 isomers are also found to have distinct distributions (Figure 6A). In this instance, however, both *n*-7 and *n*-9 forms arise from SCD-1 activity but differ by starting substrate, requiring either FA 16:0 or FA 18:0, respectively. In some regions across the tissue, signals consistent with a third DB isomer, the FADS2 metabolite PC 34:1*n*-10, were detected, but abundances were insufficient to map distribution. Challenges in characterizing less abundant metabolites are inherent to the MALDI-MSI technique (due to small sampling volumes), and therefore, to increase the signal, lipids were extracted from homogenized PCa tissues and subjected to direct infusion electrospray ionisation (ESI)-OzID analysis. Examination of lipid standards under identical conditions provided benchmarks for false-positive signals, thus confirming the presence of PC 34:1*n*-10 at low abundance in PCa tissues (Figure 6B, green). Analogous DB analysis of selected monounsaturated PS and PE lipids also unveiled them as carriers of the unusual *n*-10 isomer within PS 36:1 and PE

36:1 (Figure 6B, red and orange). Interestingly, signals arising from PE 34:1*n*-10 (blue) were insignificantly differentiated from background, indicating that incorporation of the *n*-10 FA may vary between lipid class and composition.

Examination of profiles from polyunsaturated lipids in PCa tissue extracts revealed that a previously unreported *n*-7 isomer was present alongside the highly active signaling lipid, PI 38:4*n*-6 (Epand, 2017). The use of high-resolution MS and OzID allowed for the unambiguous assignment of PI 38:4*n*-7 (cf. Figure S5; Table S6). The ratio of signals arising from this lipid and the canonical PI 38:4*n*-6 are displayed in Figure 6C, which reveals that tissue and PCa cell line extracts display PI 38:4*n*-7 around 10%–15% above any background signal arising from the *n*-6 synthetic standard. Further evidence for apocryphal desaturation in PI 38:4 was obtained by comparison to (and between) PCa cell line lipid extracts (Figure 6C) and PCa cell line fatty acyl DB analysis (Figure 4B). These findings present the existence of the *n*-10 monounsaturated FAs and *n*-7 polyunsaturated FA within human primary prostate tumors. This finding implies changes to desaturase enzyme activity or expression across tumor tissues, which, in turn, impacts lipids associated with intracellular membrane structures and signals (Bratton et al., 1997; Cocco et al., 2015; Williams et al., 2011).

DISCUSSION

Origin and consequence of desaturation plasticity

Exploration of FA DBs within cancer cell lipids in combination with gene silencing and isotope tracing experiments has revealed that mammalian cellular fatty acyl modification is far more dynamic than previously considered. It is important to note that the flow chart represented in Figure 5 presents the metabolic capabilities of mammalian cells, with some FA families arising due to extreme metabolic stress (e.g., SCD-1 gene silencing allowing FADS1 *n*-13 formation). Because cancer is known to be severely disruptive to cellular fatty acyl metabolism, however, it stands to reason that this expanded network of possibilities for FA modification provides plasticity for changes to lipid uptake or FA enzyme expression in PCa cells and tumor tissue.

Although SCD-1 and FADS2 largely show preference for canonical Δ9 and Δ6 sites during primary desaturation, a change in substrate availability and/or enzyme expression can coax a plastic response from the FADS2 enzyme—potentially yielding a much wider array of mono- and polyunsaturated FA isomers. For example, relative to the normal prostate BPH-1 cells, PC-3 cancer cells display a significant change in expression of SCD-1 and FADS2 (cf. Figure 1D), which in turn has a large downstream effect on the isomeric complexity expressed within the mono- and polyunsaturated FAs of PC-3 compared with that of BPH-1 (cf. Figure 4B). Furthermore, if substrate availability is altered in combination with these enzyme expression/activity differences, FADS2 (and possibly FADS1) plasticity allows for substrate acceptance usually observed in sebocytes (e.g., FADS2 Δ6-desaturation of 14:0, 16:0, and 18:0 to yield *n*-8, *n*-10, and *n*-12, respectively) or even changes to the enzyme-substrate complex to result in an alternative site of desaturation (e.g., FADS2 Δ8-desaturation of 18:0 to yield 18:1*n*-10). The metabolic similarity to sebum is an interesting point to ponder; sebum only contains these unusual FADS2 metabolites because sebocytes lack the expression of SCD-1 (Ge et al., 2003). One reason for this may be because SCD-1 desaturation is an oxygen-dependent reaction, meaning the oxygen-independent FADS2 can more finely regulate desaturation reactions for lipid homeostasis in the oxygen-rich environment of the skin. Given the hypoxic conditions of some tumorous tissues, it is logical to think that the SCD-1 reaction would become limited (Röhrig and Schulze, 2016) and thereby cause the upregulation of FADS2 to allow adoption of primary desaturation behaviors alongside its role in polyunsaturation events. This would account for the increase in FADS2 expression seen in the transcripts of cancer cell lines (Figure 1D), the unusual desaturation products observed (Figures 1C and 4B), and the increase in polyunsaturated FA products observed (Figure 4A). Similarly, under metabolic stress, SCD-1 and FADS1 also displayed plasticity toward substrate preference to allow for the formation of *n*-5, *n*-11, and *n*-13 FA families, further demonstrating cancer's propensity to adapt.

As has been shown in previous studies into cancer and normal prostate cell lines, a strong distinction is created when observing the differences of FA 18:1 DB isomers from the hydrolyzed FA pool (Ma et al., 2016b). These differences pertain to a change in either substrate availability or substrate preference by the SCD-1 enzyme, which in turn causes a statistically significant increase of the FA 18:1*n*-9 isomeric fraction (relative to the FA 18:1*n*-7) within cancer cells. More recently, in a study of human breast cancer and adjacent non-tumorous tissues, it was shown that a small number of sum composition phospholipids displayed a minor but statistically significant change in abundance (Wenpeng et al., 2019). The authors were then able to show that (1) discerning the DB location greatly increased the significance of the phenotypic distinction and (2) the phospholipids from cancer tissues contained a much higher proportion of the 18:1*n*-9 fatty acyl chain than the 18:1*n*-7. Here, we were able to show that the elucidation of DB positions in the context of complex lipids served to further improve phenotypic distinction while simultaneously providing a rich fingerprint for metabolic activity in PCa tissues. Furthermore, similar to the findings in breast cancer tissue, we were able to show that epithelial cancer cells in prostate tissue also contained higher proportions of *n*-9 in PC 34:1 (cf. Figure 6A). This feature of aberrant SCD-1 behavior, however, was also marked by the absence of usual FADS2 polyunsaturated FA metabolites and perhaps indicates FADS2 plasticity with a change toward primary desaturation. The *n*-10 FA metabolites associated with this enzyme plasticity were not observed in the imaging of PC 34:1 but instead were found in other phospholipid classes, suggesting that, similar to PCa cell lines, these unusual FAs are unevenly distributed among phospholipid subclasses. *n*-10 Phospholipids and other metabolites generated by FADS2 plasticity were detected in all clinical prostate specimens; however, no linear relationship was observed between the presence of *n*-10 phospholipids and percentage tumor content. As all tissues examined (Figures 6A and 6C) were derived from radical prostatectomy specimens containing PCa, it is not possible to disentangle if unusual FADS2 activity is a general

feature of prostate epithelial cells or specific to unhealthy (i.e., cancer, field-cancerization, or premalignant aberrations in histologically benign tissue) prostate cell function. Further experimentation and comparison to tumor-free prostate tissue derived from healthy prostate (obtained at cystoprostatectomy) and benign prostatic hyperplasia will provide further insight into this distinction and hence clinical utility.

From cell line studies, we were able to reveal that all FA metabolites formed from apocryphal desaturation activity were active substrates for elongation, and ELOVL2 was shown as a candidate in further diversifying the *n*-10 family. This finding is perhaps an ode to the canonical role of ELOVL2 in elongating FADS2-modified dietary fatty acyl metabolites (Guillou et al., 2010), which may suggest co-localization or co-activity between enzymes. Instead of these unusual FA metabolites being regarded by cellular machinery as malformed or unusable, they are functionalized through incorporation into known membrane and signaling phospholipid classes. As further indication toward a functional role, these unusual FA metabolites are found to be unevenly associated with certain phospholipid subclasses compared to others (cf. Figure 2; Table S4). Given that DB location will modulate inter-molecular forces and thus membrane properties (Lorent et al., 2020; Renne and de Kroon, 2018; Scanferlato et al., 2019), here it is speculated that the different isomer profiles of each phospholipid class will promote distinctive membrane fluidities among the organelles. Interestingly, activation of mTOR promotes FADS2 expression (Triki et al., 2020), opening the possibility that these systems may work together to tune lipid isomer populations to assist proliferation and resist apoptosis. For example, changes in membrane fluidity could promote mitosis for cancer cell stemness (Li et al., 2017) or hinder apoptosis triggered by PS outer-leaflet exposure (Bratton et al., 1997) or ferroptosis (Tousignant et al., 2020). Similarly, the synthesis of entirely *de-novo*-synthesized polyunsaturated FAs, such as FA 20:4*n*-7, bear remarkable similarity to biologically active FA metabolites and are being incorporated into known signaling phospholipids. Consequently, this may disrupt homeostatic lipid signaling or, indeed, fulfill usual signaling roles in the absence of dietary FA uptake or other chemical environment changes. Although further work is required to specify the biological impact that unusual lipid unsaturation has on cells, the experimental workflows and findings presented throughout this body of work serve as a roadmap toward future discovery.

STAR★METHODS

Detailed methods are provided in the online version of this paper and include the following:

- KEY RESOURCES TABLE
- RESOURCE AVAILABILITY
  - Lead contact
  - Materials availability
  - Data and code availability
- EXPERIMENTAL MODEL AND SUBJECT DETAILS
  - Human tissues
  - Cell culturing
- METHOD DETAILS
  - Lipid nomenclature
  - Tissue sectioning and mounting
  - Haematoxylin and Eosin Staining
  - Gene silencing by siRNA and enzyme inhibition
  - ^{13}Carbon tracing
  - RNA extraction and quantitative real-time polymerase chain reaction (qRT-PCR)
  - Western blot confirmation method
  - Lipid extraction
  - AMPP derivatisation
  - Gas chromatography – pooled fatty acyl analysis
  - MALDI-MSI OzID for lipid double bond imaging
  - Direct infusion ESI-OzID of lipid double bonds
  - Direct infusion ESI-OzID of pooled fatty acid double bonds (AMPP+ derivatization)
  - Conventional lipidomics for phospholipid profiles
- QUANTIFICATION AND STATISTICAL ANALYSIS
  - Gas chromatography – pooled fatty acyl analysis
  - MALDI-MSI OzID for lipid double bond imaging
  - Direct infusion ESI-OzID of lipid double bonds and pooled fatty acid double bonds (AMPP+)
  - Conventional lipidomics for phospholipid profiles
  - Statistics and error analysis

SUPPLEMENTAL INFORMATION

Supplemental information can be found online at https://doi.org/10.1016/j.celrep.2021.108738.

ACKNOWLEDGMENTS

Part of this study was supported by the Movember Foundation, the Prostate Cancer Foundation of Australia and the Australian Government Department of Health through a Movember Revolutionary Team Award, and an Australian Government grant. Other data were obtained at the Central Analytical Research Facility operated by the Institute for Future Environments and supported by funding from the Science and Engineering Faculty (QUT, Brisbane, Australia). This work was supported through funding from the Australian Research Council (DP150101715, LP180100238, and DP190101486) and an Australian Government RTP scholarship. A.P.B., R.M.A.H., and S.R.E. are grateful for funding from Interreg V EMR and the Netherlands Ministry of Economic Affairs within the "EURLIPIDS" project (EMR23).

AUTHOR CONTRIBUTIONS

Conceptualization, R.S.E.Y., M.C.S., S.J.B.; methodology, R.S.E.Y., V.R.N., R.G., D.L.M., B.L.J.P., S.R.E., M.C.S., S.J.B.; software, R.S.E.Y.; validation, R.S.E.Y., A.P.B., K.D.T., V.R.N., M.C.S.; formal analysis, R.S.E.Y., M.C.S.; investigation, R.S.E.Y., A.P.B., E.D.W., K.D.T., C.L.B., M.C.S.; data curation, R.S.E.Y.; writing – original draft, R.S.E.Y.; writing – review & editing, R.S.E.Y., E.D.W., D.L.M., B.L.J.P., R.M.A.H., M.C.S., S.J.B.; visualization, R.S.E.Y.; project administration, R.S.E.Y., M.C.S., S.J.B.; resources, E.D.W., B.L.J.P., C.C.N., S.R.E., R.M.A.H., S.J.B.; funding acquisition, B.L.J.P., C.C.N., S.R.E., R.M.A.H., S.J.B.; supervision, M.C.S., S.J.B.

DECLARATION OF INTERESTS

MALDI-MSI OzID technology was developed through an industry linkage supported by Waters Corporation and the Australian Research Council (LP180100238). S.J.B. holds patents on ozone-induced dissociation technology ("A method for the determination of the position of unsaturation in a compound," US8242439 and US7771943).

Received: September 17, 2020
Revised: November 18, 2020
Accepted: January 19, 2021
Published: February 9, 2021

REFERENCES

Bai, Y., McCoy, J.G., Levin, E.J., Sobrado, P., Rajashankar, K.R., Fox, B.G., and Zhou, M. (2015). X-ray structure of a mammalian stearoyl-CoA desaturase. Nature *524*, 252–256.

Barré, F., Rocha, B., Dewez, F., Towers, M., Murray, P., Claude, E., Cillero-Pastor, B., Heeren, R., and Porta Siegel, T. (2019). Faster raster matrix-assisted laser desorption/ionization mass spectrometry imaging of lipids at high lateral resolution. Int. J. Mass Spectrom. *437*, 38–48.

Beloribi-Djefaflia, S., Vasseur, S., and Guillaumond, F. (2016). Lipid metabolic reprogramming in cancer cells. Oncogenesis *5*, e189.

Biswas, S., Lunec, J., and Bartlett, K. (2012). Non-glucose metabolism in cancer cells—is it all in the fat? Cancer Metastasis Rev. *31*, 689–698.

Bollinger, J.G., Thompson, W., Lai, Y., Oslund, R.C., Hallstrand, T.S., Sadilek, M., Turecek, F., and Gelb, M.H. (2010). Improved sensitivity mass spectrometric detection of eicosanoids by charge reversal derivatization. Anal. Chem. *82*, 6790–6796.

Bratton, D.L., Fadok, V.A., Richter, D.A., Kailey, J.M., Guthrie, L.A., and Henson, P.M. (1997). Appearance of phosphatidylserine on apoptotic cells requires calcium-mediated nonspecific flip-flop and is enhanced by loss of the aminophospholipid translocase. J. Biol. Chem. *272*, 26159–26165.

Cocco, L., Follo, M.Y., Manzoli, L., and Suh, P.G. (2015). Phosphoinositide-specific phospholipase C in health and disease. J. Lipid Res. *56*, 1853–1860.

Collins, J.M., Neville, M.J., Hoppa, M.B., and Frayn, K.N. (2010). De novo lipogenesis and stearoyl-CoA desaturase are coordinately regulated in the human adipocyte and protect against palmitate-induced cell injury. J. Biol. Chem. *285*, 6044–6052.

Currie, E., Schulze, A., Zechner, R., Walther, T.C., and Farese, R.V., Jr. (2013). Cellular fatty acid metabolism and cancer. Cell Metab. *18*, 153–161.

Enoch, H.G., Catalá, A., and Strittmatter, P. (1976). Mechanism of rat liver microsomal stearyl-CoA desaturase. Studies of the substrate specificity, enzyme-substrate interactions, and the function of lipid. J. Biol. Chem. *251*, 5095–5103.

Epand, R.M. (2017). Features of the Phosphatidylinositol Cycle and its Role in Signal Transduction. J. Membr. Biol. *250*, 353–366.

Fahy, E., Subramaniam, S., Murphy, R.C., Nishijima, M., Raetz, C.R.H., Shimizu, T., Spener, F., van Meer, G., Wakelam, M.J.O., and Dennis, E.A. (2009). Update of the LIPID MAPS comprehensive classification system for lipids. J. Lipid Res. *50*, S9–S14.

Fritz, V., Benfodda, Z., Rodier, G., Henriquet, C., Iborra, F., Avancès, C., Allory, Y., de la Taille, A., Culine, S., Blancou, H., et al. (2010). Abrogation of de novo lipogenesis by stearoyl-CoA desaturase 1 inhibition interferes with oncogenic signaling and blocks prostate cancer progression in mice. Mol. Cancer Ther. *9*, 1740–1754.

Ge, L., Gordon, J.S., Hsuan, C., Stenn, K., and Prouty, S.M. (2003). Identification of the delta-6 desaturase of human sebaceous glands: expression and enzyme activity. J. Invest. Dermatol. *120*, 707–714.

Green, C.D., Ozguden-Akkoc, C.G., Wang, Y., Jump, D.B., and Olson, L.K. (2010). Role of fatty acid elongases in determination of de novo synthesized monounsaturated fatty acid species. J. Lipid Res. *51*, 1871–1877.

Guijas, C., Meana, C., Astudillo, A.M., Balboa, M.A., and Balsinde, J. (2016). Foamy Monocytes Are Enriched in cis-7-Hexadecenoic Fatty Acid (16:1n-9), a Possible Biomarker for Early Detection of Cardiovascular Disease. Cell Chem. Biol. *23*, 689–699.

Guillou, H., Zadravec, D., Martin, P.G.P., and Jacobsson, A. (2010). The key roles of elongases and desaturases in mammalian fatty acid metabolism: Insights from transgenic mice. Prog. Lipid Res. *49*, 186–199.

Hancock, S.E., Maccarone, A.T., Poad, B.L.J., Trevitt, A.J., Mitchell, T.W., and Blanksby, S.J. (2019). Reaction of ionised steryl esters with ozone in the gas phase. Chem. Phys. Lipids *221*, 198–206.

He, Z., Zhang, R., Jiang, F., Zhang, H., Zhao, A., Xu, B., Jin, L., Wang, T., Jia, W., Jia, W., and Hu, C. (2018). FADS1-FADS2 genetic polymorphisms are associated with fatty acid metabolism through changes in DNA methylation and gene expression. Clin. Epigenetics *10*, 113.

Hsu, L.-C., Wen, Z.-H., Chen, H.-M., Lin, H.-T., Chiu, C.-M., and Wu, H.-C. (2013). Evaluation of the Anti-Inflammatory Activities of 5,8,11-cis-Eicosatrienoic Acid. Food Sci. Nutr. *04*, 113–119.

Jakobsson, A., Westerberg, R., and Jacobsson, A. (2006). Fatty acid elongases in mammals: their regulation and roles in metabolism. Prog. Lipid Res. *45*, 237–249.

Li, J., Condello, S., Thomes-Pepin, J., Ma, X., Xia, Y., Hurley, T.D., Matei, D., and Cheng, J.-X. (2017). Lipid Desaturation Is a Metabolic Marker and Therapeutic Target of Ovarian Cancer Stem Cells. Cell Stem Cell *20*, 303–314.e5.

Liebisch, G., Vizcaíno, J.A., Köfeler, H., Trötzmüller, M., Griffiths, W.J., Schmitz, G., Spener, F., and Wakelam, M.J.O. (2013). Shorthand notation for lipid structures derived from mass spectrometry. J. Lipid Res. *54*, 1523–1530.

Lorent, J.H., Levental, K.R., Ganesan, L., Rivera-Longsworth, G., Sezgin, E., Doktorova, M., Lyman, E., and Levental, I. (2020). Plasma membranes are asymmetric in lipid unsaturation, packing and protein shape. Nat. Chem. Biol. *16*, 644–652.

Ma, X., Chong, L., Tian, R., Shi, R., Hu, T.Y., Ouyang, Z., and Xia, Y. (2016a). Identification and quantitation of lipid C=C location isomers: A shotgun lipidomics approach enabled by photochemical reaction. Proc. Natl. Acad. Sci. USA *113*, 2573–2578.

Ma, X., Zhao, X., Li, J., Zhang, W., Cheng, J.X., Ouyang, Z., and Xia, Y. (2016b). Photochemical Tagging for Quantitation of Unsaturated Fatty Acids by Mass Spectrometry. Anal. Chem. *88*, 8931–8935.

Marquardt, A., Stöhr, H., White, K., and Weber, B.H.F. (2000). cDNA cloning, genomic structure, and chromosomal localization of three members of the human fatty acid desaturase family. Genomics *66*, 175–183.

Marshall, D.L., Pham, H.T., Bhujel, M., Chin, J.S.R., Yew, J.Y., Mori, K., Mitchell, T.W., and Blanksby, S.J. (2016). Sequential Collision- and Ozone-Induced Dissociation Enables Assignment of Relative Acyl Chain Position in Triacylglycerols. Anal. Chem. *88*, 2685–2692.

Marshall, D.L., Criscuolo, A., Young, R.S.E., Poad, B.L.J., Zeller, M., Reid, G.E., Mitchell, T.W., and Blanksby, S.J. (2019). Mapping Unsaturation in Human Plasma Lipids by Data-Independent Ozone-Induced Dissociation. J. Am. Soc. Mass Spectrom. *30*, 1621–1630.

Mason, P., Liang, B., Li, L., Fremgen, T., Murphy, E., Quinn, A., Madden, S.L., Biemann, H.-P., Wang, B., Cohen, A., et al. (2012). SCD1 inhibition causes cancer cell death by depleting mono-unsaturated fatty acids. PLoS One *7*, e33823.

Matyash, V., Liebisch, G., Kurzchalia, T.V., Shevchenko, A., and Schwudke, D. (2008). Lipid extraction by methyl-tert-butyl ether for high-throughput lipidomics. J. Lipid Res. *49*, 1137–1146.

Moon, Y.A., Shah, N.A., Mohapatra, S., Warrington, J.A., and Horton, J.D. (2001). Identification of a mammalian long chain fatty acyl elongase regulated by sterol regulatory element-binding proteins. J. Biol. Chem. *276*, 45358–45366.

Nicolaides, N. (1974). Skin lipids: their biochemical uniqueness. Science *186*, 19–26.

Obukowicz, M.G., Welsch, D.J., Salsgiver, W.J., Martin-Berger, C.L., Chinn, K.S., Duffin, K.L., Raz, A., and Needleman, P. (1998). Novel, selective delta6 or delta5 fatty acid desaturase inhibitors as antiinflammatory agents in mice. J. Pharmacol. Exp. Ther. *287*, 157–166.

Paine, M.R.L., Poad, B.L.J., Eijkel, G.B., Marshall, D.L., Blanksby, S.J., Heeren, R.M.A., and Ellis, S.R. (2018). Mass Spectrometry Imaging with Isomeric Resolution Enabled by Ozone-Induced Dissociation. Angew. Chem. Int. Ed. Engl. *57*, 10530–10534.

Park, W.J., Kothapalli, K.S.D., Reardon, H.T., Lawrence, P., Qian, S.-B., and Brenna, J.T. (2012). A novel FADS1 isoform potentiates FADS2-mediated production of eicosanoid precursor fatty acids. J. Lipid Res. *53*, 1502–1512.

Park, H.G., Engel, M.G., Vogt-Lowell, K., Lawrence, P., Kothapalli, K.S., and Brenna, J.T. (2018). The role of fatty acid desaturase (FADS) genes in oleic acid metabolism: FADS1 Δ7 desaturates 11-20:1 to 7,11-20:2. Prostaglandins Leukot. Essent. Fatty Acids *128*, 21–25.

Pauter, A.M., Olsson, P., Asadi, A., Herslöf, B., Csikasz, R.I., Zadravec, D., and Jacobsson, A. (2014). Elovl2 ablation demonstrates that systemic DHA is endogenously produced and is essential for lipid homeostasis in mice. J. Lipid Res. *55*, 718–728.

Poad, B.L.J., Pham, H.T., Thomas, M.C., Nealon, J.R., Campbell, J.L., Mitchell, T.W., and Blanksby, S.J. (2010). Ozone-induced dissociation on a modified tandem linear ion-trap: observations of different reactivity for isomeric lipids. J. Am. Soc. Mass Spectrom. *21*, 1989–1999.

Poad, B.L.J., Green, M.R., Kirk, J.M., Tomczyk, N., Mitchell, T.W., and Blanksby, S.J. (2017). High-Pressure Ozone-Induced Dissociation for Lipid Structure Elucidation on Fast Chromatographic Timescales. Anal. Chem. *89*, 4223–4229.

Poad, B.L.J., Marshall, D.L., Harazim, E., Gupta, R., Narreddula, V.R., Young, R.S.E., Duchoslav, E., Campbell, J.L., Broadbent, J.A., Cvačka, J., et al. (2019). Combining Charge-Switch Derivatization with Ozone-Induced Dissociation for Fatty Acid Analysis. J. Am. Soc. Mass Spectrom. *30*, 2135–2143.

Renne, M.F., and de Kroon, A.I.P.M. (2018). The role of phospholipid molecular species in determining the physical properties of yeast membranes. FEBS Lett. *592*, 1330–1345.

Röhrig, F., and Schulze, A. (2016). The multifaceted roles of fatty acid synthesis in cancer. Nat. Rev. Cancer *16*, 732–749.

Scanferlato, R., Bortolotti, M., Sansone, A., Chatgilialoglu, C., Polito, L., De Spirito, M., Maulucci, G., Bolognesi, A., and Ferreri, C. (2019). Hexadecenoic Fatty Acid Positional Isomers and De Novo PUFA Synthesis in Colon Cancer Cells. Int. J. Mol. Sci. *20*, 832.

Schmittgen, T.D., and Livak, K.J. (2008). Analyzing real-time PCR data by the comparative C(T) method. Nat. Protoc. *3*, 1101–1108.

Schulze, A., and Harris, A.L. (2012). How cancer metabolism is tuned for proliferation and vulnerable to disruption. Nature *491*, 364–373.

Tamura, K., Makino, A., Hullin-Matsuda, F., Kobayashi, T., Furihata, M., Chung, S., Ashida, S., Miki, T., Fujioka, T., Shuin, T., et al. (2009). Novel lipogenic enzyme ELOVL7 is involved in prostate cancer growth through saturated long-chain fatty acid metabolism. Cancer Res. *69*, 8133–8140.

Thomas, M.C., Mitchell, T.W., Harman, D.G., Deeley, J.M., Nealon, J.R., and Blanksby, S.J. (2008). Ozone-induced dissociation: elucidation of double bond position within mass-selected lipid ions. Anal. Chem. *80*, 303–311.

Tousignant, K.D., Rockstroh, A., Poad, B.L.J., Talebi, A., Young, R.S.E., Taherian Fard, A., Gupta, R., Zang, T., Wang, C., Lehman, M.L., et al. (2020). Therapy-induced lipid uptake and remodeling underpin ferroptosis hypersensitivity in prostate cancer. Cancer Metab. *8*, 11.

Triki, M., Rinaldi, G., Planque, M., Broekaert, D., Winkelkotte, A.M., Maier, C.R., Janaki Raman, S., Vandekeere, A., Van Elsen, J., Orth, M.F., et al. (2020). mTOR Signaling and SREBP Activity Increase FADS2 Expression and Can Activate Sapienate Biosynthesis. Cell Rep. *31*, 107806.

Vriens, K., Christen, S., Parik, S., Broekaert, D., Yoshinaga, K., Talebi, A., Dehairs, J., Escalona-Noguero, C., Schmieder, R., Cornfield, T., et al. (2019). Evidence for an alternative fatty acid desaturation pathway increasing cancer plasticity. Nature *566*, 403–406.

Wallis, J.G., and Browse, J. (1999). The Δ8-desaturase of Euglena gracilis: an alternate pathway for synthesis of 20-carbon polyunsaturated fatty acids. Arch. Biochem. Biophys. *365*, 307–316.

Wenpeng, Z., Donghui, Z., Qinhua, C., Junhan, W., Zheng, O., and Yu, X. (2019). Online photochemical derivatization enables comprehensive mass spectrometric analysis of unsaturated phospholipid isomers. Nat. Commun. *10*, 79.

Williams, D.S., Bird, M.J., Jorissen, R.N., Yu, Y.L., Walker, F., Zhang, H.H., Nice, E.C., and Burgess, A.W. (2011). Correction: Nonsense Mediated Decay Resistant Mutations Are a Source of Expressed Mutant Proteins in Colon Cancer Cell Lines with Microsatellite Instability. PLoS One *6*, 10.1371/annotation/53805ecf-7d10-4d99-9cec-f27f5e0d4166.

Zadra, G., Photopoulos, C., and Loda, M. (2013). The fat side of prostate cancer. Biochim. Biophys. Acta *1831*, 1518–1532.

Zhang, S., and Lin, X. (2019). Lipid Acyl Chain *cis* Double Bond Position Modulates Membrane Domain Registration/Anti-Registration. J. Am. Chem. Soc. *141*, 15884–15890.

STAR★METHODS

KEY RESOURCES TABLE

REAGENT or RESOURCE	SOURCE	IDENTIFIER
Antibodies		
Rabbit / IgG polyclonal anti-FADS2	Invitrogen	Cat. # PA5-87765; RRID: AB_2804393
Biological samples		
Right and left prostate lobes obtained from the radical prostatectomy of 8 male adult human patients	This paper	N/A
Chemicals, peptides, and recombinant proteins		
Methanol (LC-MS grade)	Fischer Scientific	Cat. # A456-500
Acetonitrile (ACN; Optima®)	Fischer Scientific	Cat. # A955-500
Water (Optima®)	Fischer Scientific	Cat. # W6500
N,N-dimethyl formamide (DMF)	Fischer Scientific	Cat. # D119-500
Methyl tert-butyl ether (MTBE; HPLC grade)	Fischer Scientific	Cat. # E127-4
Hydrochloric acid (HCl; 37% in water)	Sigma-Aldrich	Cat. # 320331
Anhydrous sodium acetate (NaOAc)	Sigma-Aldrich	Cat. # W302406
Ammonium acetate (NH_4OAc)	Sigma-Aldrich	Cat. # 431311
Trimethylsulfonium hydroxide (TMSH; LiChropure®)	Sigma-Aldrich	Cat. # 92732
Tetrabutylammonium hydroxide (TBAOH; 40 wt. % in water)	Sigma-Aldrich	Cat. # 178780
Dibutylhydroxytoluene (BHT)	Sigma-Aldrich	Cat. # B1378
Chloroform (HPLC grade)	Sigma-Aldrich	Cat. # 650498
Methanol (LC-MS grade; solely for MALDI-MS based experiments)	Sigma-Aldrich	Cat. #106035
2,5-dihydroxyacetophenone (DHA; $\geq$ 99.5%, Ultra pure)	Sigma-Aldrich	Cat. # D3638
Harris Haematoxylin	Australian Biostain P/L	Cat. # AHHPAH
Ethanol 100% AR	Chem Supply Australia	Cat. # EA043
0.25% Eosin Y (certified C.C. # 45380)	ProSciTech	Cat. # C0975
Xylene mix of iosomer AnalaR	Point Of Care Diagnostics	Cat. # VWRC28975.325
Roswell Park Memorial Institute (RPMI) 1640 medium	Thermo Fisher	Cat. # 11875101
Foetal bovine serum (FBS)	Invitrogen	Cat. # F9665
RNAiMAX lipofectamine reagent	Thermo Fisher	Cat. # 13778030
SC26196 (FADS2Δ6 inhibitor) 98%	Sigma-Aldrich	Cat. # PZ0176
TOFA (combination SCD-1Δ9/ACC1 inhibitor) 98%	Sigma-Aldrich	Cat. # T6575
SPLASH Lipid-o-mix®	Avanti Polar Lipids	Cat. # 330707
Nonadecanoic acid 98%	Sigma-Aldrich	Cat. # N5252
PS 16:0/18:1n-9	Avanti Polar Lipids	Cat. # 840034
PE 18:0/18:1n-9	Avanti Polar Lipids	Cat. # 850758
PC 16:0/18:1n-9	Avanti Polar Lipids	Cat. # 792453
PI 18:0/20:4n-6	Avanti Polar Lipids	Cat. # 850144
$^{13}C_{16}$-palmitic acid 99%	Sigma-Aldrich	Cat. # 605573
$^{13}C_{18}$-stearic acid 99%	Sigma-Aldrich	Cat. # 605581
DNase/RNase-free distilled water	Thermo Fisher	Cat. # 10977015
SYBR-Green Master Mix	Thermo Fisher	Cat. # A46109
Tris-Hydrochloride (Tris-HCl)	Sigma-Aldrich	Cat. # RES3098T-B7
Sodium Chloride	Sigma-Aldrich	Cat. # S3014

(*Continued on next page*)

Continued

REAGENT or RESOURCE	SOURCE	IDENTIFIER
Triton X-100	Sigma-Aldrich	Cat. # T8787
Sodium deoxycholate	Sigma-Aldrich	Cat. # 30970
cOmplete EDTA-free protease inhibitor	Roche	Cat. # COEDTAF-RO
Sodium fluoride 99%	Sigma-Aldrich	Cat. # S6776
Sodium orthovanadate 99.99%	Sigma-Aldrich	Cat. # 450243
Sodium pyrophosphate 99% (BioUltra)	Sigma-Aldrich	Cat. # 71501
β-glycerophosphate	Sigma-Aldrich	Cat. # G9422
NuPAGETM 4-12% Bis-Tris SDS-PAGE Protein Gels	Thermo Fisher	Cat. # NP0329BOX
n-Hexane, 95%, Optima	Fisher Scientific	Cat. # H306-1
AMP+ Mass Spectrometry Kit	Cayman Chemical	Cat. # 710000
37 FAMES mix	Restek	Cat. # 35077
Methyl-nonadecanoate	Sigma-Aldrich	Cat. # 74208
Critical commercial assays		
Pierce BCA Protein Assay kit	Thermo Fisher	Cat. # BCA1
RNEasy mini kit	QIAGEN	Cat. # 74104
SensiFast cDNA synthesis kit	Bioline	Cat. # BIO-65053
Deposited data		
Raw and analyzed data	This paper	Deposited to QUT Research Data Finder https://doi.org/10.25912/RDF_1611708145189
Experimental models: cell lines		
Human prostate cancer cells (lymph metastasis): LNCaP clone FGC (RRID:CVCL_0395)	American Type Cell Culture Collection (ATCC®)	ATCC® CRL-1740
Human prostate cancer cells (vertebral metastasis): VCaP (RRID:CVCL_2235)	American Type Cell Culture Collection (ATCC®)	ATCC® CRL-2876
Human prostate cancer cells (bone metastasis): PC-3 (RRID:CVCL_0035)	American Type Cell Culture Collection (ATCC®)	ATCC® CRL-1435
Human prostate cancer cells (CNS metastasis): DU145 (RRID:CVCL_0105)	American Type Cell Culture Collection (ATCC®)	ATCC® HTB-81
Human primary prostate cells (immortalized by HPV RNA transfection): RWPE-1 (RRID:CVCL_3791)	American Type Cell Culture Collection (ATCC®)	ATCC® CRL-11609
Human primary prostate cells (benign hyperplasia): BPH-1 (RRID:CVCL_1091)	Gifted by P. J. Russell and J. Clements (Australian Prostate Cancer Centre-Queensland, Australia)	N/A
Oligonucleotides		
FADS2 FADS2fwd: CCCGGCACAACTTACACA FADS2rev: CCATGCTTGGCACATAGACACTT	Sigma-Aldrich	SASI_Hs01_00029610, SASI_Hs01_00029612, SASI_Hs01_00029608
SCD1 SCD1fwdexon4: CCAGCTGTCAAAGAGAAGG SCD1frevexon5: AAATACCAGGGCACAAGC	Sigma-Aldrich	SASI_Hs01_00029617, SASI_Hs01_00181377, SASI_Hs01_00181371
ELOVL2 ELOVL2fwdexon5: GTGTGTCTTGAACTGGATACC ELOVL2revexon6: TCCACCAAAGATACTTGTGC	Sigma-Aldrich	SASI_Hs01_00018935
ELOVL3 ELOVL3fwdexon2: CTACATGAAGGAACGCAAGG ELOVL3revexon3: ACACGGTTTGCTTTAGGC	Sigma-Aldrich	SASI_Hs01_00086480

(*Continued on next page*)

Continued

REAGENT or RESOURCE	SOURCE	IDENTIFIER
ELOVL6	Sigma-Aldrich	SASI_Hs01_00242071
ELOVL6fwdexon2: GAAGCCATTAGTGCTCTGG		
ELOVL6revexon3: ACAAACTGACTGCTTCAGG		
MISSION® siRNA Universal Negative Control #1	Sigma-Aldrich	Cat# SIC001
Software and algorithms		
Image Studio Lite	LI-COR® Biotechnology	N/A
Xcalibur (v 3.0.63)	Thermo Scientific	N/A
MassLynx 4.2 MS software	Waters	N/A
Analyst® software	Sciex	N/A
GCMSsolution (postrun analysis) Software	Shimadzu	N/A
Lipidview software	Sciex	N/A
High Definition Imaging (HDI; v 1.4)	Waters	N/A
Python peak fitting script	This paper	N/A
R x64 3.6.1	The R Foundation	N/A
Other		
CM 1950 Cryostat	Leica Biosystems	N/A
Glass slides (SuperFrost® plus) Menzel-Gläser	Thermo Scientific	Cat. # 4951PLUS4
Coverslips (Tissue-Tek® Glas)	Sakura Finetek	Cat. # 9580
Tissue-Tek Prisma slide scanner	Sakura Finetek	N/A
Pannoramic Digital slide scanner	3DHistech	N/A
TC20 Automated Cell Counter	Bio-Rad	N/A
NanoDrop ND-1000 Spectrophotometer	Thermo Scientific	N/A
ViiA-7 Real-Time PCR system	Applied Biosystems	N/A
Bolt Mini Blot Module	Thermo Scientific	N/A
Li-Cor® Odyssey imaging system	LI-COR® Biotechnology	N/A
TQ8040 GC/MS	Shimadzu	N/A
RTX-2330 capillary column	Restek	
HTX TM-Sprayer	HTXImaging	N/A
Sublimator	HTXImaging	N/A
prototype μMALDI source	Barré et al., 2019	N/A
Synapt G2-*Si* HDMS mass spectrometer	Waters	N/A
Ozone generator (solely for MALDI-MS experiments)	Ozone Solutions	TG-40 gen 2
Ozone monitor	2B Technologies	106-H
Orbitrap Elite high-resolution mass spectrometer	Thermo Scientific	N/A
Ozone generator	Absolute Ozone	Titan-30UHC
Triversa Nanomate	Advion	N/A
High pressure liquid chromatograph	Shimadzu	LC-20A HPLC
QTRAP 6500 hybrid triple quadrupole/LIT mass spectrometer	Sciex	N/A

RESOURCE AVAILABILITY

Lead contact

Further information and requests for resources and reagents should be directed to and will be fulfilled by the Lead Contact, Stephen Blanksby (stephen.blanksby@qut.edu.au).

Materials availability

All reagents generated in this study are available from the Lead Contact with a completed Materials Transfer Agreement.

Data and code availability

The datasets generated during and/or analyzed during the current study are available as a data archive from QUT Research Data Finder using the following DOI: https://doi.org/10.25912/RDF_1611708145189

EXPERIMENTAL MODEL AND SUBJECT DETAILS

Human tissues

Prostate tissues were collected with ethical approval of the St. Vincent's Hospital Human Ethics Committee and in accordance with Australian National Health and Medical Research Council Guidelines. Tissues samples were collected from radical prostatectomy specimens by a pathologist, immediately snap frozen in liquid nitrogen, and stored at −80°C. Both right and left lobes were collected from adult human-males. Age is not reported as samples were deidentified and are not linked to any donor information.

Cell culturing

LNCaP (RRID: CVCL_0395), VCaP (RRID: CVCL_2235), PC-3 (RRID: CVCL_0035), DU145 (RRID: CVCL_0105) and RWPE-1 (RRID: CVCL_3791) cells were obtained from the American Type Cell Culture Collection (ATCC; Manassas, Virginia, USA), while BPH-1 (RRID: CVCL_1091) was gifted by P. J. Russell and J. Clements (Australian Prostate Cancer Centre-Queensland, Australia). All cell lines were cultured in Roswell Park Memorial Institute (RPMI) medium (Thermo Fisher, Waltham, MA, USA) supplemented with 5% fetal bovine serum (FBS, Invitrogen, Waltham, MA, USA) and incubated at 37°C in 5% CO2. Medium was changed every 3 days, and cells were passaged at approximately 80% confluency by trypsinisation. Cell lines were authenticated using genotyping in March 2018 by Genomics Research Centre (Brisbane, Australia) and routinely tested to exclude mycoplasma infection. Cell number and viability was determined by trypan blue staining and using a TC20 Automated Cell Counter (Bio-Rad).

METHOD DETAILS

Lipid nomenclature

Lipid nomenclature was based on previously defined shorthand naming systems that only state the level of molecular detail that is known (Fahy et al., 2009; Liebisch et al., 2013). In short, the lipid category is defined by a two-letter abbreviation (e.g., PC; phosphatidylcholine) followed by the number of carbons and DBs in the fatty acids separated by a colon (e.g., a PC with 34 carbons and 2 DBs; PC 34:2). If further analysis has been undertaken to reveal individual fatty acid composition but not the stereospecific number on the glycerol backbone (*i.e., sn*-position), this can be indicated with an underscore (i.e., PC 16:0_18:2). Instead, if *sn*-position is known fatty acids can be separated by a forward-slash (*i.e., sn-1/sn-2*; PC 16:0/18:2). For established positions, the digit indicating the number of DBs is directly followed by the *n*-number when referencing the number of carbons distal to the methyl terminus (i.e., PC 16:0/18:2*n*-6) or the bracketed Δ-number when referencing the carboxylate terminus (i.e., PC 16:0/18:2(*Δ9*)). It should be noted that a single position given in polyunsaturated series implies methylene interruption of subsequent DBs (i.e., PC 16:0/18:2*n*-6 = PC 16:0/18:2*n*-6,9). A table of fatty acyl common names and shorthand nomenclature equivalents is provided in Table S1.

Tissue sectioning and mounting

Using a CM 1950 Cryostat (Leica Biosystems, Nussloch, Germany), tissue biopsies were sectioned at 10 μm thickness using a blade that was free from optimal cutting temperature (OCT) compound and fixed on standard glass slides (SuperFrost +, Menzel-Gläser, Braunschweig, Germany) using 10% neutral buffered formalin for 30 s prior to MALDI-MS imaging protocol (refer to method "MALDI-MSI OzID for lipid double bond imaging") and the hematoxylin and eosin (H&E) staining protocol (refer to method "Haematoxylin and Eosin Staining"). Tissue slides for MALDI-MSI were placed into a sealed slide holder and purged with nitrogen gas before being stored on dry ice for inter-laboratory shipping.

Haematoxylin and Eosin Staining

Tissue H&E staining took place after sectioning/mounting using an autostainer (Tissue-Tek Prisma, Sakura Finetek, Torrance, CA, USA) according to the following sequence: tissues were washed with water for 2 minutes before being exposed to hematoxylin (Harris Haematoxylin (PAH), Australian Biostain P/L, Traralgon, Australia) for 5 minutes. "Bluing" was achieved with water rinsing for 4 minutes and exposed for 10 s to ethanol (Chem Supply Gilman, Australia) acidified with 1% HCl before 5 minutes of further rinsing with water. Eosin staining (0.25% Eosin Y; certified C.C. # 45380, ProSciTech, Kirwan, Australia) took place for 2 minutes before 40 s of water rinsing. One 80% ethanol rinse followed by two 100% ethanol rinses then took place for 45 s, 30 s and 45 s, respectively. Triplicate xylene (Point Of Care Diagnostics, North Rock, Australia) washes were then conducted for 1 minute each. Coverslips (Tissue-Tek Glas, Sakura Finetek, Torrance, CA, USA) were then applied before imaging using a Pannoramic Digital slide scanner (3DHistech, Hungary) for histopathological analyses.

Gene silencing by siRNA and enzyme inhibition

LNCaP cells were seeded at $1.2x10^5$ cells/well in 6-well plates. After 48 hours, cells were transfected with 10 nM siRNAs (Sigma-Aldrich) targeting SCD-1 (SASI_Hs01_00029617, SASI_Hs01_00181377, SASI_Hs01_00181371), FADS2 (SASI_Hs01_00029610,

SASI_Hs01_00029612, SASI_Hs01_00029608), ELOV2 (SASI_Hs01_00018935), ELOVL3 (SASI_Hs01_00086480), and ELOVL6 (SASI_Hs01_00242071). Off-target effects were controlled using a scrambled siRNA control sequence (SIC001, Sigma-Aldrich) at 10 nM. Before forward transfection, growth medium was replaced with 1 mL serum free medium (RPMI 1640), and transfection solution using RNAiMAX lipofectamine reagent was prepared according to the manufacturer's instructions (Thermo Fisher). Following six hours of transfection, FBS was added to the medium to a final concentration of 5%, and cells were grown for 72 hours. For direct inhibition of enzyme activity, 2 million cells were treated for 72 hours with the indicated concentrations of SC26196 (FADS2Δ6 inhibitor, 30 μM in DMSO, Sigma-Aldrich) and 5-tetradecyloxy-2-furoic acid (TOFA; combination SCD-1Δ9 /ACC1 inhibitor, 5 μM in DMSO, Sigma-Aldrich). Cell assay titrations for inhibitor concentrations can be found in Figure S3.

^{13}Carbon tracing

For ^{13}C tracing studies, LNCaP cells were chosen due to their heightened FADS2 expression. Cells were seeded and cultured under the conditions mentioned previously (refer to experimental model "Cell culturing"). After 48 hours of seeding, cells were switched to fresh media supplemented with either unlabeled (i.e., $^{12}C_{16}$-palmitic acid) or labeled (i.e., $^{13}C_{16}$-palmitic acid or $^{13}C_{18}$-stearic acid) fatty acids conjugated to bovine serum albumin (BSA) at a final concentration of 20 μM. All fatty acids were purchased from Sigma Aldrich, Castle Hill, Australia. Cells were grown for a further 72 hours and washed twice with ice-cold phosphate buffered saline (PBS) before lipid extraction.

RNA extraction and quantitative real-time polymerase chain reaction (qRT-PCR)

Cells seeded in 6 well plates were grown in 5% FBS to a confluency of 70% before RNA extraction using the RNEasy mini kit (QIAGEN, Hilden, Germany) following the manufacturer's instructions. RNA concentration was measured using a NanoDrop ND-1000 Spectrophotometer (Thermo Scientific, Waltham, MA, USA). 2 μg of total RNA was used to prepare cDNA with SensiFast cDNA synthesis kit (Bioline) according to the manufacturer's instructions and diluted 1:6 with DNase/RNase-free water (Thermo Fisher, Waltham, MA, USA). qRT-PCR was performed with SYBR-Green Master Mix (Thermo Fisher Scientific, Waltham, MA, USA) using the ViiA-7 Real-Time PCR system (Applied Biosystems, Forster City, CA, USA). Determination of relative mRNA levels was calculated using the comparative ΔΔCt method (Schmittgen and Livak, 2008), where expression levels were normalized relative to that of the housekeeping gene receptor-like protein 32 (RPL32) for each treatment and calculated as fold change relative to the expression levels of BPH-1 cells. All experiments were performed in triplicate and analysis and statistics were performed with Microsoft Excel. Primer sequences can be found in in the Key resources table).

Western blot confirmation method

Cell seeding and gene silencing of FADS2 was carried out as described above. Protein extracts for western blotting were generated from whole cell lysates prepared in lysis buffer [50 mM Tris, HCl pH 7.6, 150 mM sodium chloride, 1% Triton X-100, 0.5% sodium deoxycholate, 0.1% SDS, one cOmplete EDTA-free Protease Inhibitor Cocktail tablet (Roche) per 10 mL, phosphatase inhibitors sodium fluoride (30 mM), sodium pyrophosphate (20 mM), β-glycerophosphate (10 mM), and sodium orthovanadate (1 mM)]. Before lysis in 250 μL buffer on ice for 5 minutes, cells were washed twice with ice-cold PBS. Protein extracts were cleared by centrifugation for 10 minutes at 20,000 x g at 4°C and transferred into fresh tube. Protein concentration was measured using Pierce BCA Protein Assay kit according to manufacturer's instructions (Thermo Fisher Scientific, Waltham, MA, USA). 20 μg of total protein/lane were separated by SDS-polyacrylamide gel electrophoresis (SDS-PAGE) using NuPAGE 4%–12% Bis-Tris SDS-PAGE Protein Gels (Thermo Fisher Scientific), and western blot was completed using the Bolt Mini Blot Module (Thermo Fisher Scientific) according to the manufacturer's instructions. After transfer and blocking of polyvinylidene fluoride (PVDF) membranes (Immobilon) in 5% BSA TBS Tween-20 buffer (Thermo Fisher Scientific), primary antibody directed against FADS2 (PA5-87765; RRID: AB_2804393, Thermo Fisher Scientific) was applied overnight at 4°C at a dilution of 1:1000 followed by probing with the appropriate Odyssey fluorophore-labeled secondary antibody and visualization on the Li-Cor® Odyssey imaging system (LI-COR® Biotechnology, NE, USA). Protein expression levels were quantified using Image Studio Lite (LI-COR® Biotechnology), normalized relative to the indicated housekeeping protein, and expressed as fold-changes relative to the control treatment.

Lipid extraction

Cell and homogenized tissue lipids were extracted using methods similar to those described by Matyash et al., 2008 and were quantifiable through the use of internal standards in the form of deuterated lipids (SPLASH Lipid-o-mix, Avanti Polar Lipids, Alabaster, USA) and an odd-chain fatty acid found to be not present within the samples (nonadecanoic acid, Sigma Aldrich, Munich, Germany). To minimize pipetting error, a stock internal standard solution was made in bulk using 720 μL MTBE (0.01% BHT), 40 μL SPLASH Lipid-o-mix® and 20 μL nonadecanoic acid in MTBE (3.35 mM) per 2 M cells. Cell pellets in 2 mL clear glass vials (~2M cells) were twice washed with PBS solution, before adding 220 μL of methanol and 780 μL of the prepared internal standard stock solution. Capped vials were vortexed for 20 s, before 1.5 h bench-top agitation. Phase separation was induced by adding 200 μL of aqueous ammonium acetate (150 mM) before samples were vortexed for 20 s and centrifuged for 5 min at 2,000 x g. The organic supernatant was pipetted off to a clean labeled 2 mL glass vial and stored at −20°C before analyses.

AMPP derivatisation

100 μL of the lipid extract was dried under nitrogen gas in 4 mL glass vials. Fatty acids were hydrolysed from lipids using 1:1 methanol:tetrabutylammonium hydroxide (40 wt. % in water) and heating at 85°C for 2 h before allowing to cool to room temperature. 1.5 mL of water (Optima®) was added to each of the vials and acidified with 120 μL of 5 M aqueous hydrochloric acid to achieve a pH of 2. Biphasic extraction of the supernatant was then undertaken using two separate aliquots (1 mL) of n-hexane to optimize the recovery of fatty acids. The individual sample supernatant fractions were combined and dried under nitrogen to yield fatty acids. The obtained fatty acids were then functionalised with AMPP+ using an AMP+ Mass Spectrometry Kit (Cayman Chemical, Ann Arbor, MI) and following a similar method discussed by Bollinger et al. (2010). Briefly, 150 μL of 4:1 ACN:DMF was added to the hydrolysed lipid samples prepared above, followed by 10 μL of 1-ethyl-3-(3-dimethylaminopropyl)carbodiimide (EDC●HCl; 1 M in water), 20 μL of 1-hydroxybenzotriazole (5 mM in 99:1 ACN:DMF), and 20 μL of AMPP+ coupling reagent (15 mM in ACN). The resulting solution was sealed, vortexed for 1 min and heated at 65°C for 30 min. After cooling to room temperature, the reaction mixtures were diluted with water (1 mL) and saturated aqueous NH_4Cl (50 μL); mixtures were then twice extracted using MTBE (2 × 1 mL). The MTBE supernatants were combined and stored in sealed 2 mL vials at −20°C before MS analysis. 5 μL of the Restek 37 mix of FAMEs and blanks were also derivatised through the above method and were used as experimental quality-controls.

Gas chromatography – pooled fatty acyl analysis

A reference standard of 38 fatty acid methyl ester standards was prepared by mixing a purchased 37 fatty acid methyl ester (FAME) standard (Restek, Bellefonte, PA, USA) and 450 μM methyl-nonadecanoate in MTBE (Sigma Aldrich) at a 1:9 ratio. Samples were prepared for analysis by mixing sample extracted lipids 5:1 with TMSH. Pooled batch quality controls (PBQC) and blanks were used throughout for quality control and data reliability.

Samples were analyzed using a TQ8040 GC/MS (Shimadzu, Kyoto, Japan) with chromatographic separation being carried out through an RTX-2330 capillary column (cyanopropyl stationary phase, 60 m x 0.25 mm, 0.20 μm film thickness; Restek). GC/MS instrument conditions were then optimized for FAME separation (He carrier gas, column flow of 2.6 mL/min, 22:1 split ratio, 1 μL sample injections, injector temperature of 220°C, interface and ion source temperature of 250°C). To shorten the total experiment duration and assist with chromatographic separation, a 30-minute column oven temperature gradient was used (150°C initial temperature with a 10°C/min increase to 170°C, followed by a 2°C/min increase to 200°C and a further 1.3°C/min increase to 211°C where the temperature was held for the remaining 5 minutes of the experiment). Column eluents were then subject to 70 eV of source energy for electron ionisation and ions were detected by Q3 scan mode over a *m/z* 50-650 range.

MALDI-MSI OzID for lipid double bond imaging

10 μm tissue sections mounted on standard glass slides were first thinly coated with 12 passes (45 mm spray height, 30°C, 10 psi, 2 mm track spacing) of 100 mM sodium acetate (2:1 methanol/chloroform) via an HTX TM-Sprayer (HTXImaging, Chapel Hill, NC, USA). Sample slides were then coated with 2,5-DHA via sublimation (40 mg, 160°C, 4 minutes) using a sublimator (HTXImaging, Chapel Hill, NC, USA). Coated sample slides were then loaded into a prototype μMALDI source (Barré et al., 2019) (Nd:YAG laser operating at 1.5 kHz, producing 25 nJ pulses at 355 nm; Waters, Wilmslow, England) for sample desorption and ionisation. 50 μm^2 pixels were sampled at a velocity of 2.0 mm/s with a 1.62 A laser diode current. Samples were analyzed using a Synapt G2-*Si* HDMS mass spectrometer (Waters, Wilmslow, England) modified with a closed loop ozone generation system to deliver ozone (up to 18% w/w in oxygen) to the ion mobility gas inlet of the instrument, as described previously (Poad et al., 2017). Ozone was generated from oxygen feed gas (99.999% purity, Linde Gas Benelux BV, the Netherlands) using a high concentration ozone generator (TG-40 gen 2, Ozone Solutions, Hull, IA, USA) and the concentration measured online using a UV-absorption based ozone monitor (106-H, 2B Technologies, Boulder, CO). The mass spectrometer was operated in ion-mobility mode, resulting in a reaction time with ozone of ~15 ms, corresponding to the ion-mobility drift time. The quadrupole mass filter was set to transmit m/z 782 (i.e., $[PC\ 34:1+Na]^+$ and $[PC\ 36:4+H]^+$) which was subsequently allowed to react with ozone in the ion mobility cell to yield OzID fragmentation. The resulting monoisotopic ions (precursors and products) were then mass analyzed by time of flight (nominal resolution 15,000).

Direct infusion ESI-OzID of lipid double bonds

The DBs of intact glycerophospholipids were determined via mass spectrometry using a modified Orbitrap Elite high-resolution mass spectrometer (Thermo Scientific, Bremen, Germany) capable of ozone-induced dissociation. Briefly, ozone was produced via a high-concentration generator (Titan-30UHC Absolute Ozone, Edmonton, Canada) and was introduced into the helium buffer gas flow before conduction through to the high-pressure region of the linear ion trap (LIT) (Paine et al., 2018). Similarly, a diverter valve was placed on the nitrogen gas inlet to the higher collisional dissociation (HCD) cell, and nitrogen was replaced with generated ozone gas (Marshall et al., 2019).

Operating in positive-ion mode for PC lipid OzID, cell line lipid extract samples were mixed 1:1 (v/v) with 500 μM methanolic sodium acetate solution and introduced to the mass spectrometer via a chip-based nano-electrospray source (TriVersa Nanomate, Advion, Ithaca, NY, USA) using 1.35 kV/0.35 psi spray parameters. Using the Thermo Xcalibur software package, a data independent acquisition sequence was created to perform sequential OzID (activation time (AT) = 2 s (HCD), collision energy (CE) = 1 V) and CID/OzID (MS^2: AT = 30 ms (LIT), normalized collision energy (NCE) = 40; MS^3: AT = 1 s, NCE = 0) for 9 sodiated

phosphatidylcholine precursor ion masses with a maximum injection time of 100 ms, isolation window of ± 0.5 Da across a 175-1000 Da scan range. Included sodiated precursor ion *m/z* values were: 754.6, 780.6, 782.6, 804.6, 806.6, 808.6, 810.6, 830.6 and 832.6. This method was also used to assign DBs within lipids that were labeled with stable-isotope fatty acids, with the only method modification being the precursor ion masses that were selected. For PCs labeled with heavy-palmitate or heavy-stearate three labeled and three unlabeled lipids were submitted for OzID and CID/OzID analysis (*m/z* 754, 770, 782, 798, 810 and 826; and *m/z* 754, 772, 782, 800, 810 and 826, respectively). The product ions from all fragmentation experiments were detected using the orbitrap mass analyzer for high resolution and accurate mass, allowing for unambiguous assignment of characteristic fragments to specific lipids and not isobaric lipids or isotopes. Intensity values obtained from OzID and CID/OzID mass spectrometric experiments were the average of 24 and 39 scans, respectively. Adapting the work of Marshall et al. (2016) and Hancock et al. (2019) and the aforementioned positive-ion mode experiments, MS^3 experiments were created for TG and CE related scans, respectively (*cf.* Table S4). In brief, for TGs, sodiated precursor ions were mass selected and underwent activated OzID in the linear ion trap (MS^2: NCE = 27, AT = 2 s), with subsequent monounsaturated fatty acid related product ions undergoing OzID in the HCD cell (MS^3: CE = 1 V, AT = 5 s) before high resolution detection. For CEs, precursor ions first underwent activated OzID in the linear ion trap (MS^2: NCE = 2, AT = 500 ms) before the $[M+Na+16]^+$ product ion was mass selected to undergo further activated OzID and detection in the linear ion trap (MS^3: NCE = 1, AT = 5 s).

Operating in negative-ion mode for PE, PS, PG and PI lipid OzID, cell line lipid extract samples were mixed 1:1 (v/v) with 5 mM methanolic ammonium acetate solution and introduced to the mass spectrometer via a TriVersa Nanomate, set to use −1.35 kV/0.35 psi spray parameters. Using the Thermo Xcalibur software package, 4 separate data independent acquisition sequences were created for each of the phospholipid subclasses. For each method, sequential OzID (AT = 2.5 s (HCD), CE = 1 V) and CID (MS^2: AT = 5 ms (LIT), NCE = 33-39) was performed for 9 deprotonated lipid precursor masses (totalling 36 phospholipids) with a maximum injection time of 100 ms, isolation window of ± 0.5 Da across a scan range of 200-1000 Da. Included deprotonated precursor ion *m/z* values were: (for PE) 688.5, 716.5, 742.5, 744.5, 782.5,766.5, 768.5, 770.5 and 772.5; (for PS) 732.5, 760.5, 786.5, 788.5, 806.5, 810.5, 812.5, 814.5 and 816.5; (for PG) 719.5, 747.5, 773.5, 775.5, 793.5, 797.5, 799.5, 801.5 and 803.5; and (for PI) 807.5, 835.5, 861.5, 863.5, 885.5, 887.5, 889.5, 891.5 and 915.5. The product ions from all fragmentation experiments were detected using the orbitrap mass analyzer for high-resolution mass accuracy (120,000 FWHM at 400 *m/z*), allowing for unambiguous assignment of characteristic fragments to specific lipids and not isobaric lipids or isotopes. Intensity values obtained from OzID and CID mass spectrometric experiments were averaged across 16 and 77 scans individual scans, respectively.

Using methods similar to those developed for cell line extracts, OzID was also performed on homogenized tissue lipid extracts. Due to the small quantity of tissue from which lipids were extracted, extracts were first dried under nitrogen gas and reconstituted to one quarter the volume (4-fold increase in concentration). Samples were reconstituted in either methanolic sodium acetate (500 μM) for positive-ion mode or methanolic ammonium acetate (5 mM) for negative-ion mode. Using the parameters described previously for positive-ion mode PC acquisitions, OzID and CID/OzID was performed on three PC lipids (*m/z* 754.5, 782.6 and 810.6). Resulting OzID and CID/OzID data was detected using the orbitrap mass analyzer (120,000 FWHM at 400 *m/z*) and ion intensity values were averaged across 11 and 23 scans, respectively. Given the low sample concentration and the decrease in ion detection efficiency inherent to negative-ion mode mass spectrometry, the aforementioned method to obtain OzID DB data for PE, PS, PG and PI lipids was modified. A data independent method was created to sequentially acquire OzID (AT = 10 s; NCE = 19-23) for the 32:1, 34:1 and 36:1 phospholipid compositions (12 total phospholipids) using a maximum injection time of 100 ms, isolation window of ± 0.5 Da across a scan range of 200-1000 Da. Included *m/z* values were: 688.5, 716.5, 719.5, 732.5, 744.5, 747.5, 760.5, 775.5, 788.5, 807.5, 835.5 and 863.5. To further improve detection of low intensity signals, product ion fragments were analyzed in the high-pressure region of the dual linear ion trap. Low resolution ion fragments were compared against standards run under the same conditions to improve reliability of assignments. Intensity values obtained from OzID experiments were averaged across 9 scans.

Direct infusion ESI-OzID of pooled fatty acid double bonds (AMPP+ derivatization)

Hydrolysed lipid extracts (including cell line lipids, LNCaP siRNA experiments and the fatty acid methyl ester standard mix) were derivatised with AMPP+ as described above (refer to method "AMPP derivatisation") and introduced via chip-based nano-electrospray using 1.90 kV/0.5 psi spray parameters. Using the Thermo Xcalibur software package, data independent acquisition sequences were created to perform ozonolysis within the linear ion trap (AT = 5 s, NCE = 25) for 24 fatty acid precursor ion masses with a maximum injection time of 100 ms, isolation window of ± 0.5 Da and scan range between 105-600 Da. Included precursor ion masses for AMPP+ derivatised FAs were: 14:1 (*m/z* 393.5), 14:2 (*m/z* 391.5), 15:1 (*m/z* 407.5), 16:1 (*m/z* 421.5), 16:2 (*m/z* 419.5), 16:3 (*m/z* 417.5), 17:1 (*m/z* 435.5), 18:1 (*m/z* 449.5), 18:2 (*m/z* 447.5), 18:3 (*m/z* 445.5), 19:1 (*m/z* 463.5), 20:1 (*m/z* 477.5), 20:2 (*m/z* 475.5), 20:3 (*m/z* 473.5), 20:4 (*m/z* 471.5), 20:5 (*m/z* 469.5), 20:6 (*m/z* 467.5), 22:1 (*m/z* 505.5), 22:2 (*m/z* 503.5), 22:3 (*m/z* 501.5), 22:4 (*m/z* 499.5), 22:5 (*m/z* 497.5), 22:6 (*m/z* 495.5) and 24:1 (*m/z* 533.5). Subsequent OzID product ions were then transferred through to the orbitrap mass analyzer for unambiguous assignment by high-resolution mass detection (mass resolution 120,000 (FWHM) at *m/z* 400). Ion abundance values were averaged across 11 scans.

Conventional lipidomics for phospholipid profiles

Lipid extracts from cell lines were run through an automated lipidomics workflow using an LC-20A HPLC (Shimadzu, Kyoto, Japan) set to deliver 100 μL sample loop-injections into a mobile phase of 5 mM methanolic ammonium acetate flowing at 15 μL/min. The sample column and column oven were bypassed with Viper PEEKsil (50 μm, Thermo Fisher, Waltham, MA, USA) to maintain instrument back pressure limits. Sample lipids were then directly infused through the electrospray ionisation source of a QTRAP 6500 hybrid triple quadrupole/LIT mass spectrometer (SCIEX, Concord, ON, Canada) using a spray voltage of 5 kV, a source temperature of 150°C and both source gasses set to 15 (arb.). Various precursor ion and neutral loss scans were employed to confirm lipid head group, with the detected *m/z* being indicative of summed-fatty-acyl composition. (PC: PIS *m/z* 184.2, CE: 39V; PE: NL *m/z* 141.1, CE: 29V; PS: NL *m/z* 185.1, CE: 29V; PG: NL *m/z* 189.1, CE: 29V; PI: NL *m/z* 275.1, CE: 29V; ChE: NL *m/z* 259.1, CE: 29V). Instrument blanks were run through-out to ensure no sample carry-over and pooled batch quality controls (PBQC) were used to gauge instrument performance over the duration of the experiment.

QUANTIFICATION AND STATISTICAL ANALYSIS

Gas chromatography – pooled fatty acyl analysis

Tabulated ion intensity data from the *m/z* 55 extracted ion chromatogram (XIC) was extracted from the data files using the native Shimadzu Post-run analysis software. The *m/z* 55 XIC was chosen due to the enhanced detection of monounsaturated fatty acids. To ensure detection biasing was minimal, 3-point calibration curved were created with the reference standard to obtain molar correction factors for all fatty acid species. Using a Python script that was developed inhouse, chromatographic peaks were compared with a temporal tolerance of 0.013 min against the reference standard for fatty acyl species assignment. For quantification, the slope of the peak and the maximum height (min. threshold: 0.01% of total ions) was used to fit a Gaussian distribution, which was subsequently integrated and normalized to the methyl-nonadecanoate internal standard. Previous analysis of the samples without an included internal standard revealed no detectable methyl-nonadecanoate and hence all integrated chromatographic signal was attributed to the internal standard. Pandas DataFrames were then created and exported to .csv format where Microsoft Excel was then used for the remaining cell count normalization, internal standard concentration factoring, statistical analysis, and graphing.

MALDI-MSI OzID for lipid double bond imaging

HDI software (Version 1.4, Waters, Wilmslow, England) was used for data processing and image creation by integrating positional files obtained from the μMALDI source with the Waters .raw files from the Synapt G2-*Si*. The top 200 most intense fragment ion peaks were extracted from the raw/un-normalized spectra across a mass range of 200-1000 *m/z* with an isolation window of 0.02 Da and mass resolution set to maximum (20,000). Characteristic ions for the OzID aldehyde and Criegee ions were identified and summed to show isomeric distribution of PC 34:1. Similarly for PC 36:4*n*-6, aldehyde and Criegee ions from each double bond position were summed to show the distribution across tissue. Because quantitation was not the focus of the imaging analysis, maximum gradient intensity values were individually set to assist visualization and contrast of lipid distributions. Hence, the maximum gradient values vary for each lipid species and can be observed in the linear color scale bars of Figure S1. Images were smoothed using linear interpolation and composite images were created using the in-built "Add" data blending mode, which blends co-localized colors together.

Direct infusion ESI-OzID of lipid double bonds and pooled fatty acid double bonds (AMPP+)

Averaged mass spectral data were extracted from the Thermo .raw files using Thermo Xcalibur Qual Browser (Version 3.0.63, Thermo Scientific, Bremen, Germany). Data tables were imported to Microsoft Excel where the data was normalized to the total ion count (TIC) before product ions were located and quantified. For high resolution mass spectrometry, a minimum peak intensity threshold of 0.013% of the TIC (~10:1 signal-to-noise) was put in place, and a *m/z* Δppm of 6 was used for product ion assignment validation. Translation to assignments was made according to previously published tables for OzID aldehyde and Criegee product ion neutral loss masses (Paine et al., 2018) OzID aldehyde and Criegee ion abundances were summed and represented as a fraction of the all isomer related OzID product ion signals (i.e., fractional distribution). This method of representation provides a further degree of normalization for comparison, making the fractions reflective of changes in the molar concentration of isomers.

Conventional lipidomics for phospholipid profiles

Lipidview (Version 1.3 beta, SCIEX, Concord, ON, Canada) was used for data processing of SCIEX data files obtained from the QTRAP 6500. Lipid assignments were based on the software lipid tables and shortlisted to include even-chain lipids with 0-6 s. Odd-chain/ether-lipid data was obtained but was not included in this study due to the ambiguity in assigning isobars in low resolution mass spectrometry. Isotope correction factors were applied, and MS peaks were ratioed to the isotope corrected internal standard included in each scan type. The inclusion of deuterated and odd chain fatty acids within the internal standard lipids sufficiently mass shifted internal standards away from any biological lipids, therefore allowing accurate and reliable peak intensity measurements to be discerned. Data tables were extracted from Lipidview and imported to Microsoft Excel for cell count normalization, internal standard concentration factoring, statistical analysis, and graphing.

Statistics and error analysis

The mean with 95% confidence intervals was used for error analysis on column-charts throughout and was calculated using Microsoft Excel and conventional equations. Box and whisker plots display conventionally accepted quartile values for the data minimum, 1st quartile, median, 3rd quartile and maximum. For Figures 1B and 1C, the mean and variance were calculated using Microsoft Excel to establish an independent one-tailed Welsh's t test and t-values were translated to statistical significance via relevant degrees of freedom and critical t-value tables. Remaining principal component analyses, heatmaps, and correlation matrices, including statistical significance and correlation coefficients, were calculated using R x64 3.6.1 packages and built-in functions using a Pearson product-moment correlation (i.e., PerformanceAnalytics, prcomp(), Hmisc() and corrplot()). With the exception of Figure 6, all population values (i.e., "n=") refer to cell culture replicates. The population values of Figure 6 instead refer to either the number of cell culture replicates, or the number of patient tissues used to conduct the statistical test, as indicated in the figure caption. Specific statistical details for each of the figures (including number of replicates, p value representation and error model), can be found within the respective figure captions.